T H E   U N I V E R S I T Y   O F   T U L S A

THE GRADUATE SCHOOL

EXPERIMENTS AND MODELING OF ESP PERFORMANCE WITH VISCOUS OILS AND OIL-WATER EMULSIONS

by
Jianlin Peng

A thesis submitted in partial fulfillment of

the requirements for the degree of Master of Science

in the Discipline of Petroleum Engineering

The Graduate School

The University of Tulsa

2020

THE UNIVERSITY OF TULSA

THE GRADUATE SCHOOL

EXPERIMENTS AND MODELING OF ESP PERFORMANCE WITH VISCOUS OILS AND

OIL-WATER EMULSIONS

by
Jianlin Peng

A THESIS

APPROVED FOR THE DISCIPLINE OF

PETROLEUM ENGINEERING

By Thesis Committee

Hong-Quan Zhang, Chair
Ovadia Shoham
Baojun Song
Haiwen Zhu

COPYRIGHT STATEMENT

ABSTRACT

Jianlin Peng (Master of Science in Petroleum Engineering)

Experiments and Modeling of ESP Performance with Viscous Oils and Oil-Water Emulsions

Directed by Dr. Hong-Quan Zhang

82, pp., Chapter 4: Conclusions and Recommendations

(238 words)

A General Electric (GE) TE-2700 14-stage radial type electrical submersible pump (ESP) was tested with a 3-inch closed flow loop under different viscous oil flow conditions. A pipe-in-pipe heat exchanger was used to cool down the temperature. The ISO-VG320 oil was used as a working fluid for single-phase oil tests. Tap water was added to create oil-water emulsions. At water fraction: 0 and 5%, and different rotational speeds (1800 rpm, 2400 rpm, 3000 rpm, and 3500 rpm), flowrates, pump head, and temperature were recorded, and the ESP performance was characterized. Mass flowrate and density were monitored using the mass flowmeter. Fluid samples were collected during the tests, and viscosity-temperature relationships for both single-phase oil, and oil-water emulsions were measured using a rotational rheometer. The ESP performance declined with the increase of fluid viscosity.

A mechanistic model was developed based on the Euler theory to predict ESP hydraulic performance. The head losses, including friction loss, turn loss, leakage loss, and recirculation loss, were subtracted. The friction factor correlation in the ESP performance model was modified. Compared with the original mechanistic model, predictions by the improved model show a better agreement with the experimental data at low flow rates. Emulsion rheology was modeled by considering the effects of droplet size, friction, shear, and stage number with corresponding dimensionless numbers. Results agree well with the experimental data, but additional data are required to verify the model generality in the future study.

ACKNOWLEDGMENTS

I would like to thank Dr. Hong-Quan Zhang, my advisor, for having me as his master's student and as a Research Assistant of Tulsa University Artificial Lift Projects (TUALP). Without his guidance, understanding, and support, I would not have accomplished my master's study. His wholehearted devotion to and meticulous attitude towards academic research inspired me to become a qualified researcher in the past two and a half years as well as in the future.

I would like to express my gratitude to the TUALP team for their resourcefulness and help. I thank Project Engineer Mr. Bryan Sams, for his technical advice and prompt actions to take care of my experimental facilities. I also thank Ms. Donna Trankley for her professional administrative assistance and management. I would give special thanks to Dr. Haiwen Zhu for his help in facility repair, experiment, and thesis revision. I would also give many thanks to Dr. Jianjun Zhu for his advice on the modification of the mechanistic model. I am also grateful to Dr. Yi Shi for helping me improve the flow loop and collect experimental data.

My sincere appreciation goes to Dr. Ovadia Shoham and Dr. Baojun Song for being my thesis committee members.

Last, I would like to dedicate this work to my parents, Fei Peng, and Bin Huang. Their unlimited love and support always give me strength during my academic pursuit.

TABLE OF CONTENTS

LIST OF FIGURES

LIST OF TABLES

INTRODUCTION

The electrical submersible pump (ESP) is one of the most widely used artificial lift methods in the oil industry. Compared with other artificial lift methods, ESP is more suitable for high flow rates, and it is being adopted in offshore production systems. It is used to overcome the pressure loss and lift very high liquid flow rate. A stack of centrifugal pump stages is connected by a central shaft in the ESP. Each stage has a rotational impeller and a stationary diffuser. The impeller is locked by a key to the shaft, which is rotated by a submerged motor. As a result, the liquid is accelerated and then guided by a diffuser. This way, the electric energy is transformed into hydraulic pressure energy. Only the water performance curves (head, horsepower, and efficiency) are provided by the manufacturers. However, ESP performance is affected by fluid properties, including but not limited to viscosity, density, gas fraction, and interfacial surface tension. Therefore, an accurate prediction of the ESP performance is required to optimize the production system design and operation.

Viscous effects on ESP performance has been analyzed by many researchers using different methodologies. Some researchers conducted experiments on different ESPs with varying flow conditions. Analyzing the viscous effect on a limited number of ESPs is a simple task and can characterize the pump performance within the tested ranges. However, it is difficult to predict the performance of every ESP in the market because of wide viscosity and flow ranges. Some researchers proposed empirical correlations based on experiments to avoid analyzing the complicated flow structures inside the ESP. These correlations lose accuracy in different pumps and flow conditions. CFD simulation can help understand the fluid behavior inside a pump stage, but it is very time-consuming, and the results are sometimes unreliable. Therefore, a mechanistic model, which is reliable and easy to be used, is derived in this study based on physical principles.

In the following, Chapter 1 is the literature review. Chapter 2 demonstrates the experiment facility, procedures, test matrix, and results. Chapter 3 presents the development, modification, and validation of the mechanistic model. Finally, Chapter 4 presents conclusions and recommendations.

CHAPTER 1

LITERATURE REVIEW

1.1 Ippen

Ippen (1946) directed more than 220 performance tests for oil viscosities up to 10,000 Saybolt universal second (SUS), which is around 1900 cP, with four distinctive single-stage centrifugal pumps. The pump head of different oil viscosities was measured under different rotational speeds. It is the first study of viscosity effects on pump performance in the laboratory. Ippen defined Reynolds number as

$$R_D = 2620 \frac{N d_2^2}{\nu . 10^5} \tag{1.1}$$

where N is the rotational speed of the impeller in rpm, d_2 is the impeller diameter in ft, and ν is the kinematic viscosity in cSt (centistokes).

The ratio of oil head to water head $\left(\frac{H_o}{H_w}\right)$, the efficiency loss $\left(\frac{100-e}{100}\right)$, and the ratio of oil power input to the water power input $\left(\frac{BHP_o}{s_o \cdot BHP_w}\right)$ is corrected by oil specific gravity and plotted against R_D. Pumps with R_D lower than 1,000 cannot be plotted using this method.

1.2 Stepanoff

Stepanoff (1949) conducted ESP experiments with fluid viscosities from 1 to 2,000 cSt, which is around 1800 cP. He introduced the impeller specific speed, N_s, to describe the pump characteristics under different types of fluid. N_s is defined as

$$N_s = \frac{\sqrt{q_{BEP}N}}{H_{BEP}^{0.75} g^{0.75}} \tag{1.2}$$

where q_{BEP} is pump capacity at BEP in GPM, N is the impeller rotational speed in rpm, H_{BEP} is the pump head at BEP in ft, and g is the gravitational acceleration in ft/s^2. Thus, a relation can be written as

$$\frac{q_{BEP}^{vis}}{q_{BEP}^{water}} = \left(\frac{H_{BEP}^{vis}}{H_{BEP}^{water}}\right)^{1.5} \tag{1.3}$$

The left side of Equation (1.3) can be defined as the flow rate correction factor, F_Q, and the right side of Equation (1.3) can be identified as the head correction factor.

Stepanoff defined a Stepanoff Reynolds Number:

$$Re_{Stepanoff} = 6.0345 \frac{Nq_{bep}^{vis}}{\sqrt{H_{bep}^{water}}\nu} \tag{1.4}$$

where N is the rotational speed in rpm, q_{bep}^{vis} is the viscous fluid flow rate at BEP in bpd, H_{bep}^{water} is the water head at BEP in ft, and ν is the liquid kinematic viscosity in cSt.

To obtain the hydraulic efficiency, the pump head correction factor and flow rate correction factor, as well as the Stepanoff Reynolds Number, were plotted. An iterative method was applied with an initial guess of the viscous fluid flow rate to obtain the pump performance from the plots.

1.3 Hydraulic Institute

An empirical correlation based on the catalog water curve was proposed by Hydraulic Institute (1955) for the centrifugal pump performance under viscous flow. Three correction factors are defined as

$$C_Q = \frac{q_{vis}}{q_w}, \tag{1.5}$$

$$C_H = \frac{H_{vis}}{H_w}, \tag{1.6}$$

and $$C_\eta = \frac{\eta_{vis}}{\eta_w}. \tag{1.7}$$

where C_Q, C_H, and C_η are the correction factors of flowrate, head, and efficiency, q_{vis} and q_w, H_{vis} and H_w, and η_{vis} and η_w are the flowrates, heads, and efficiencies of viscous fluid and water flow, respectively.

The correction curves can be found in the charts provided by Hydraulic Institute in a broad flow rate range. However, stand-alone experiments are recommended if high accuracy is required.

1.4 Amaral et al.

Amaral et al. (2007) conducted experiments on a semi-axial ESP and a conventional radial pump. Glycerin and water with a viscosity range from 1020 to 67 cP by changing temperatures from 20 to 60°C were tested. According to their results, the pump affinity law can roughly capture the viscosity effect on pump performance. Compared with the experimental test curves, the accuracy of the predicted curve decreases with the increase of oil viscosity.

1.5 Morrison et al.

The conventional pump affinity laws were modified by Morrison et al. (2017) to consider the oil viscosity effect. The flow behavior of a mixed type pump with different fluid viscosities ranging from 2.4 to 400 cP was investigated by using the Computational Fluid Dynamics (CFD) method. The modified flow coefficient (φ) and head coefficient (Ψ) along with Timer's rotational Reynolds number (Re_w) are defined as:

$$\varphi = \frac{Q}{\omega D_s^3}, \tag{1.8}$$

$$\Psi = \frac{\Delta P}{\rho D_s^2 \omega^2}, \tag{1.9}$$

and $$Re_w = \frac{\rho \omega D_s^2}{\mu} \tag{1.10}$$

These three dimensionless parameters follow a single universal curve:

$$\Psi = C_1 \phi {Re_w}^{-Mo} + C_2 \tag{1.11}$$

where C_1 and C_2 are empirical constants, and Mo is the Morrison number which is related to the pump specific speed. The Morrison numbers of different pump types are listed in Table 1.1.

Table 1.1 Values of Morrison Number for Different Pump Types

Pump Type	N_s	Mo
Mixed flow	2758	0.066
Split vanes	3027	0.072
Semi-axial	3817	0.2
Helical axial	5284	0.05

As shown in Figure 1.1, the modified affinity law agrees well with the experimental tests. Since the Morrison number changes a lot for different types of pumps, further investigations are necessary to verify its accuracy on other pumps.

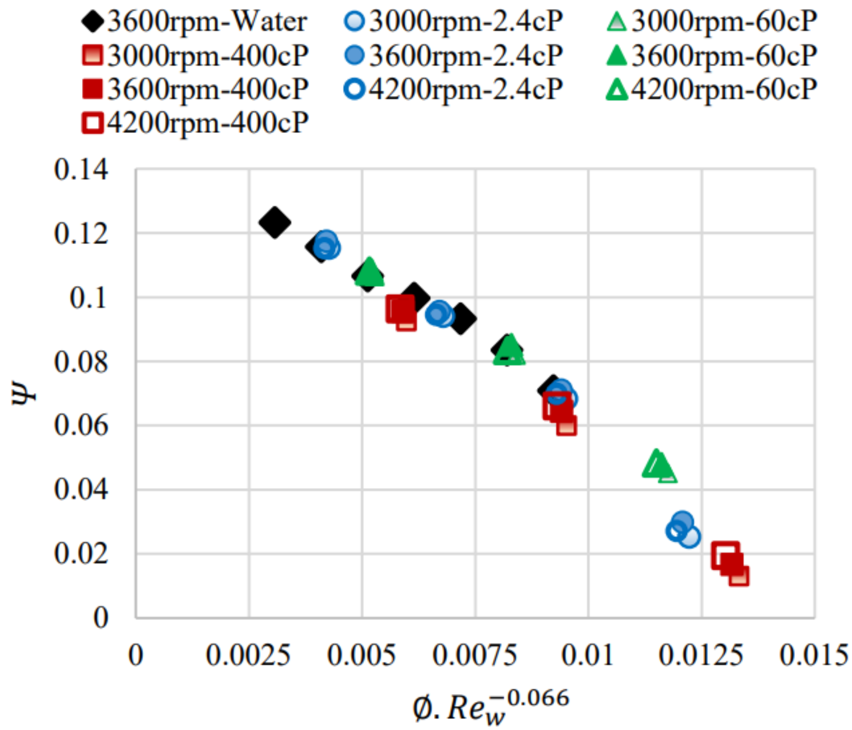

Figure 1.1 Empirical Pump Head Curve - Mixed Flow Type Pump

1.6 Phan et al.

Phan et al. (2017) presented the effects of high viscosity oil on the performance of a single-stage centrifugal pump. The Conoco R&O Multipurpose 220 oil was used as a working fluid at three temperatures: 43°C (155 cP), 46°C (134 cP), and 49°C (115 cP), and three rotational speed: 3600, 3300, and 3000 rpm. The working fluid was stored in a tank, which has a heater at the bottom, to eliminate residual gas in the flow loop. The schematic of the pump facility is shown in Figure 1.2. According to their results, the homogeneous model is unable to predict head performance with acceptable accuracy.

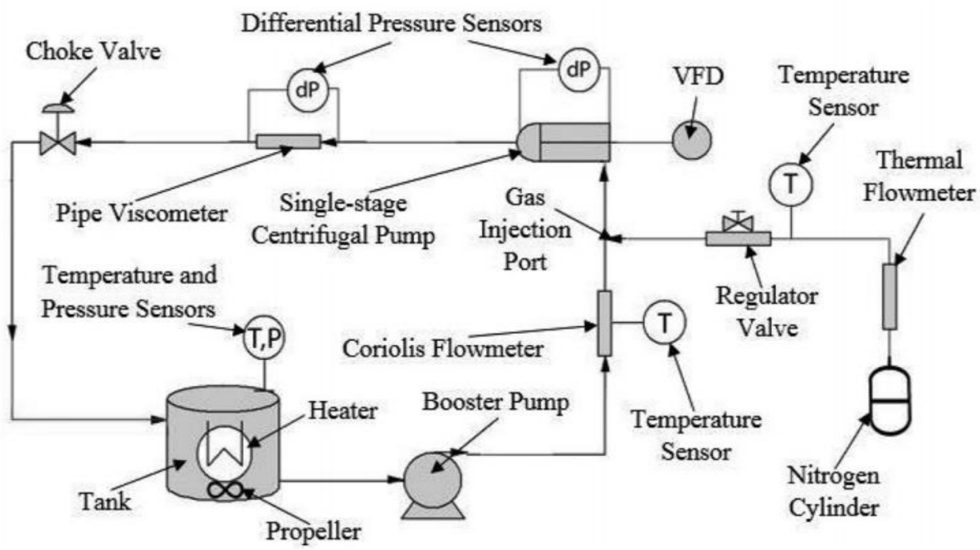

Figure 1.2 Schematic of Pump Facility of Phan et al. (2017)

CHAPTER 2

EXPERIMENTAL SETUP AND RESULTS

The experimental facility, testing procedure, data acquisition system (DAQ), and experimental results for oil and oil-water emulsions are presented in this chapter.

2.1 Experimental Facility

The schematic of the experimental facility is shown in Figure 2.1. As shown in Figure 2.2, the previous TE-2700 gas-liquid flow loop by Zhu et al. (2017a and 2017b) is upgraded for high viscosity and oil-water emulsion tests. Zhang (2017) disconnected the air injection line and the gas-liquid separator and added a pipe viscometer, as shown in Figure 2.2. ESP performance was tested with water and ND20 oil with viscosity from 1 cp to 107 cp. To discharge gas trapped inside the loop more effectively, a ball valve was connected to the gas discharge port in Figure 2.4 (a). Later on, it was replaced by a pipe, as shown in Figure 2.4 (b), to change the discharge direction downwards to protect students from breathing in the hazardous oil mist when releasing the pressure. The flow loop has a capacity of 46.3 gallons and a maximum designed flow rate of 6,000 bpd. The detailed specifications and configurations are listed in Appendix A.

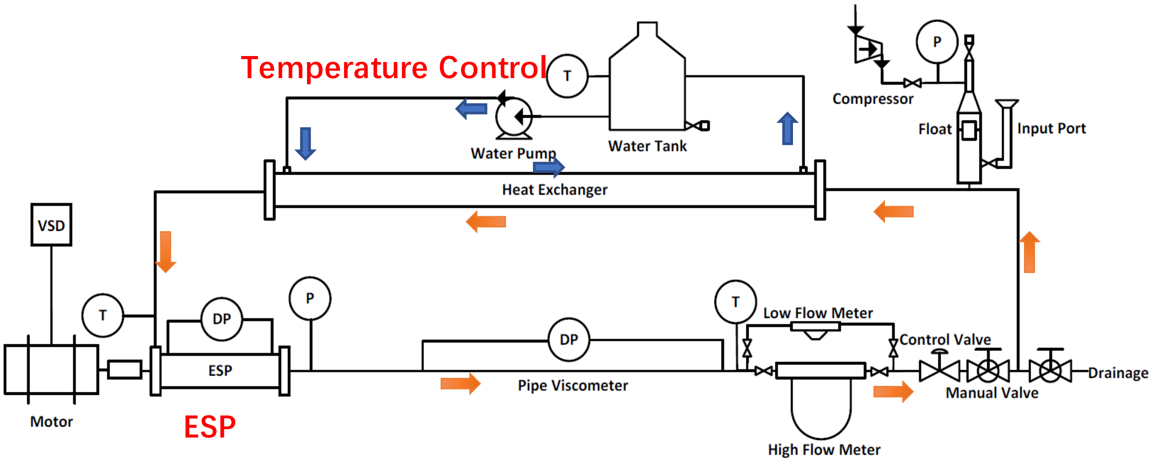

Figure 2.1 Schematic of TUALP High-Viscosity ESP Flow Loop

Figure 2.2 TUALP Gas-Liquid ESP Flow Loop

Figure 2.3 TUALP High-Viscosity ESP Flow Loop

(a) (b)

Figure 2.4 TUALP High-Viscosity Flow Loop Discharge Port

with (a) Ball Valve (b) Elbow Pipe

2.1.1 Viscous Fluid Flow Loop

In this study, ESP TE2700, which was driven by a motor (North American H3650), was tested in a 3-inch stainless steel closed loop. The rotational speed of the motor was controlled by a variable speed drive (Hitachi L300P). The pressure increments were measured using four differential pressure transducers (Rosemount 3051S). The pressure was monitored by six absolute pressure transmitters (Rosemount 2051). Three-wire platinum resistance temperature detectors (RTDs) were used to measure the temperature at the ESP intake and the ESP output, and one J-thermocouple was used to record the temperature 15-ft downstream the ESP where the fluid flow was fully developed (Zhu 2019). One pneumatic control valve and one manual control valve were installed to control the liquid flowrate. Mass flowrate and density were monitored by a Coriolis flowmeter (Proline Promass 80E).

The flow loop was pressurized before the high viscosity oil test by a compressor (Kaeser CSD60) and controlled by an air pressure regulator to avoid cavitation. In the gas discharge section, a hollow cylinder (length: 7.75-in, diameter: 2.75-in) was submerged in the 3-in pipeline as a float to prevent the reverse gas entrainment.

The heat exchanger, in which ice water was pumped by a Dayton Stainless Steel Centrifugal Pump 2ZWT9A, was initially designed to control the loop temperature. However, it was hard to maintain a stable temperature due to the thickness of the pipe. Therefore, it was mainly used to cool down the flow loop after each high viscosity test.

2.1.2 ESP for Experiment

The TE-2700 used in the experiment is a 14-stage radial type ESP manufactured by General Electric (GE) with a BEP at 2,700 bpd and 3,500 rpm. The pump bench is shown in Figure 2.5. The pressure ports were drilled at stages 2~14. The differential pressure of each stage was measured, except for stage 1. The absolute pressures at pump inlet and outlet, as well as the pressure at each stage from stages 5-12, were measured to double-check the differential pressure measurements (Zhu et al. 2018a, Zhu et al. 2019a, Zhu et al. 2019b). The rotational speed and torque were measured by a torque sensor. However, only part of the torque data was collected in this study since the torque monitor lost its accuracy in the test. The pump catalog curve from the manufacturer is shown in Figure 2.6.

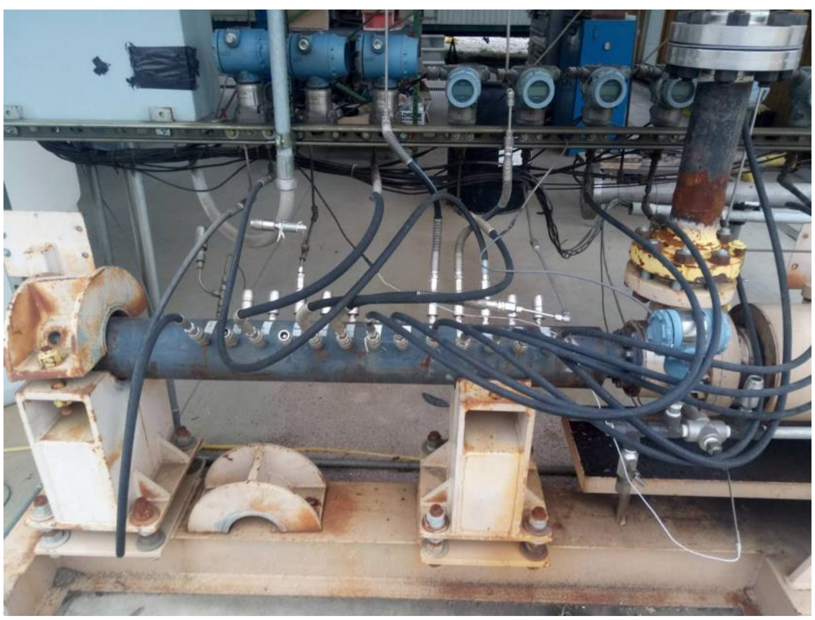

Figure 2.5 TE-2700 ESP of TUALP High Viscosity Flow Loop

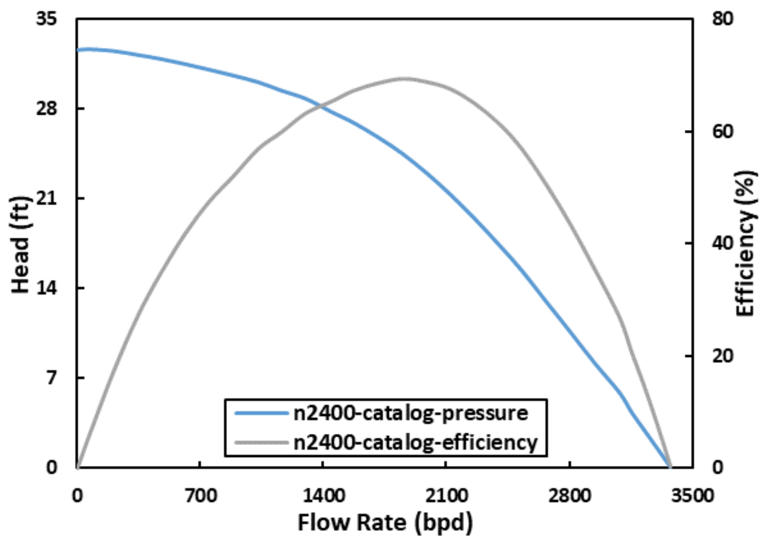

Figure 2.6 Catalog Pressure and Efficiency Curve from the Manufacturer.

2.1.3 Data Acquisition System

The data acquisition system was built by National Instrument (NI) modules. NI input modules (cFP-AI-111) were used to collect output analog signals (4~20 mA) from temperature and pressure transmitters, as well as the Coriolis flowmeter. Temperature transmitters (INOR IPAQ R520) were used to convert RTD and thermocouples' output signals to 4~20 mA current signals. A NI output module (cFP-AO-200) was used in this study to generate input signals to control the pneumatic control valve and VSD (Zhu et al. 2019c). All modules were connected to a NI Ethernet interface (cFP-1804) and transferred to a data processing computer. The analog signals were scaled up to the engineering unit by NI LabVIEW for data processing.

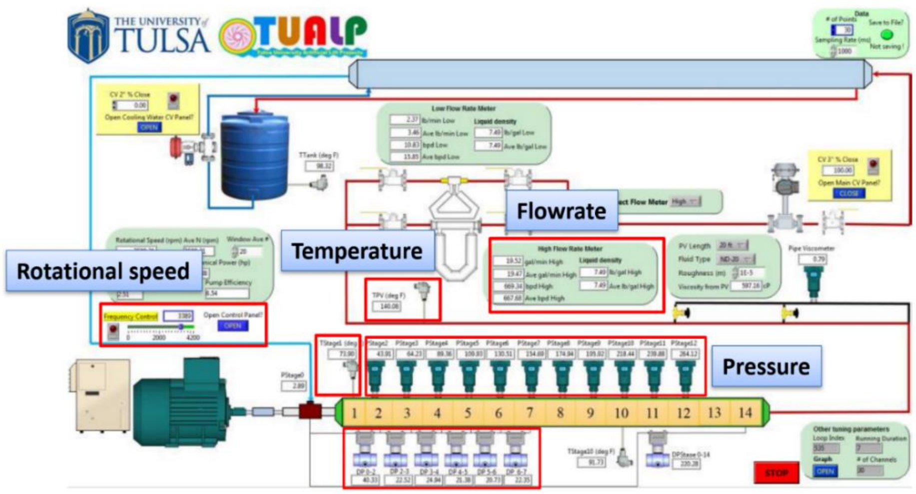

Figure 2.7 Data Acquisition System of TUALP High-Viscosity ESP Flow Loop

As shown in Figure 2.7, the DAQ program was written in a graphic-programming language LabVIEW 2014 for acquiring data and controlling the flow rate (Zhu et al. 2018b). The flow rate was controlled by adjusting the closing percentage of the pneumatic control valve, as shown in Figure 2.8. When the pneumatic control valve was not available, the flow rate is controlled by a manual control valve.

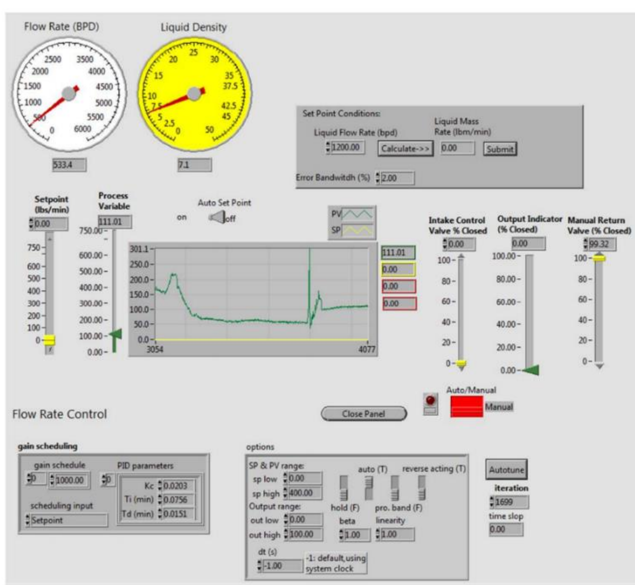

Figure 2.8 Liquid Flow Rate Control of TUALP High-Viscosity ESP Flow Loop

2.2 Experimental Program

2.2.1 Testing Fluids

Tap water and lubricating oil were used as work fluids in this study. The oil ISO-VG320 used in this study has a higher viscosity range (50 cP to 1600 cP, as shown in Figure 2.9) than that of ND20 in the previous study. Lab tests with different shear rates at 30℃, 40℃, and 70℃, as shown in Figure 2.10, indicate that this oil behaves as a Newtonian fluid.

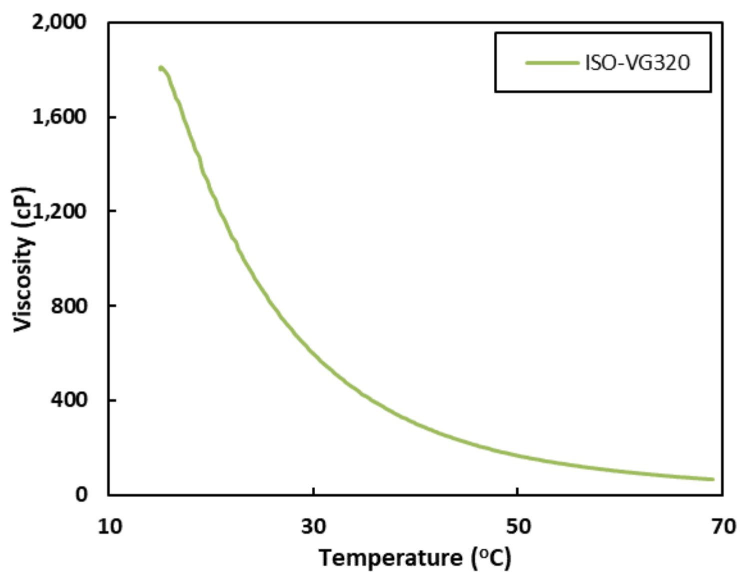

Figure 2.9 ISO-VG320 Viscosity versus Temperature

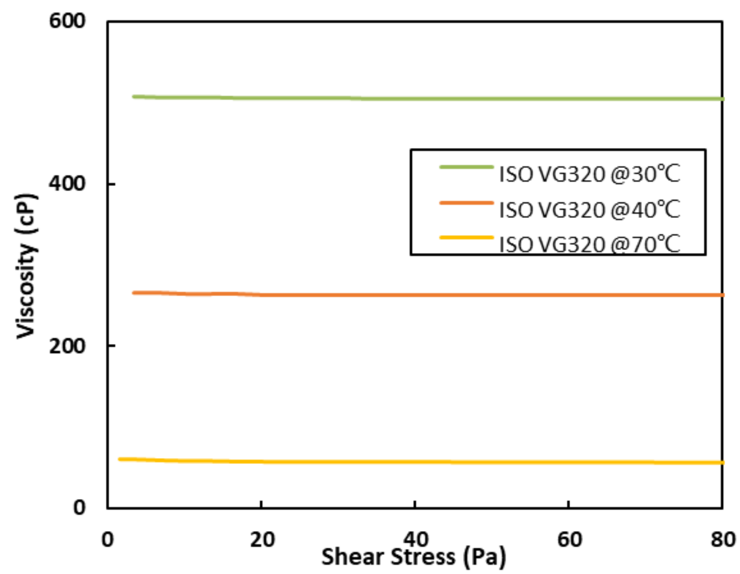

Figure 2.10 ISO-VG320 Shear Rate Tests at Different Temperatures

The emulsion was sampled from the loop and examined closely under a microscope. Figure 2.11 and Figure 2.12 show that the 5% water cut fluid has a similar property as the ISO-VG320 oil.

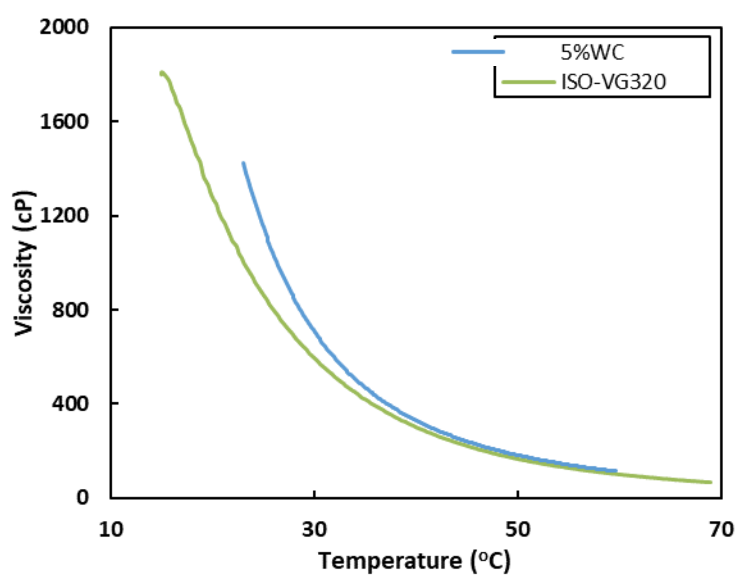

Figure 2.11 5% Water Cut and Pure Oil Viscosity versus Temperature

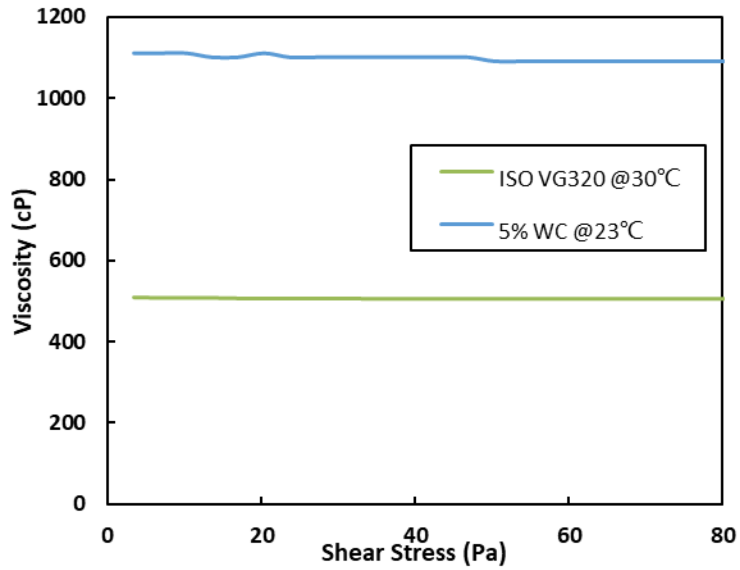

Figure 2.12 Shear Stress Test Comparison for 5% WC Emulsion and Pure Oil

2.2.2 Experimental Procedure

2.2.2.1 Single-Phase Fluid Testing Procedure.

Before the high viscosity test, the loop needs to be filled with the working fluid, and the gas bubbles in the fluid need to be removed. Therefore, the flow loop was firstly filled by working fluid through the input port until the liquid level reached the upper part of the transparent input port, while the gas discharge valve and the injection valve were open. Then, the discharge valve and injection valve were closed, and the loop was pressurized 30 psig to avoid cavitation at the pump inlet (Zhu et al. 2019d, Zhu et al. 2018c). The pump was started at a low rotational speed for a short period until gas bubbles trapped in the liquid were separated in the discharge pipe. After the pump was stopped, the loop pressure was released to vent the separated gas in the discharge pipe. Previous steps were repeated until the fluid level in the transparent liquid input port was stable, and the loop was ready for a high viscosity test.

After gas bubbles were removed by the steps as mentioned above, the flow loop was re-pressurized to 50 psig, and the rotational speed was increased to the designated point. The pump curve was recorded when the temperature was in the designed range. Pump rotational speed, temperatures, pressures, differential pressures, and flow rate were recorded every second. At each flow rate, fifty samples were collected to minimize the uncertainty. When the loop temperature was unable to be maintained by the heat exchanger, the pump was stopped, and the loop was cooled down by the heat exchanger. The pump may need to be stopped multiple times until a complete pump curve was accomplished (Zhu et al. 2018d).

2.2.2.2 Oil-Water Emulsion Testing Procedure

Emulsion experiments are very similar to the single-phase oil testing. The total loop volume, which was measured before the test, is 46.3 gallons. The water and oil volume were calculated accordingly. A stable emulsion mixture can be created by the tested ESP in a few minutes. When the readings in the mass flow meter were stable without large fluctuations, the pump curve was recorded similarly as for the single-phase oil tests.

2.2.3 Test Matrix

The test matrix is listed in Table 2.1. The experiments were interrupted by the winter conditions, followed by the COVID-19. Therefore, only the high viscosity oil test and the 5%

water-oil emulsion test were completed.

Table 2.1 Test Matrix

Fluid	Water Fraction (%)	ESP Rotational Speed (rpm)	Choke Opening (%)
Tap Water	100	2400	100, 50, 40, 30, 20, 15, 10, 9, 8, 7, 6, 5
ISO-VG320	0	1800, 2400, 3000, 3500	
	5, 10, 15, 20, 25, 30, 35, 40, 45, 50	3500	

2.3 Experimental Results

2.3.1 Sing-Phase Liquid Results

2.3.1.1 Water Performance Curve

TE-2700 ESP was tested with tap water at the rotational speed of 2,400 rpm. The pump curve is compared with the catalog curve and previous tests by Zhang (2017) in Figure 2.13. The tested pump curve agrees well with the catalog curve, which validates the experimental setup of this study.

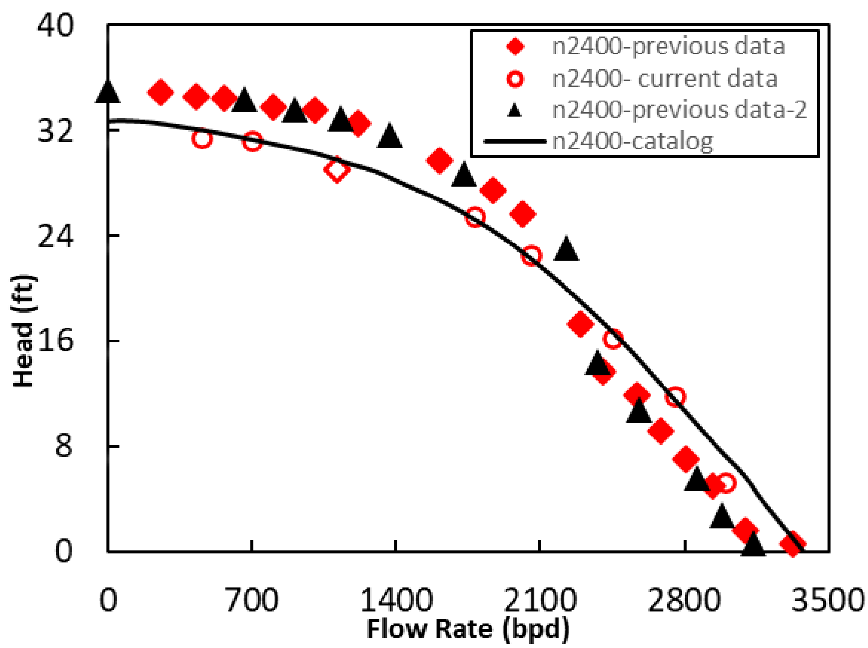

Figure 2.13 Comparison of Current, Previous Data and Catalog Curve

2.3.1.2 Oil Performance Curve

TE-2700 ESP was tested with ISO-VG320 oil at four pump rotational speeds of 1,800 rpm, 2,400 rpm, 3,000 rpm, and 3,500 rpm. The viscosity of the original ISO-VG320 sample was comparable to the samples collected from the loop, as shown in Section 2.2.1. Then, the viscosity can be obtained from the curves measured by the rotational viscometer (Anton Paar RheolabQC).

The head curves at the rotational speeds of 1,800 rpm, 2,400 rpm, 3,000 rpm, and 3,500 rpm are shown in Figure 2.14, Figure 2.15, Figure 2.16, and Figure 2.17, respectively. Their trends are similar, and the pump head decreases with the increase of fluid viscosity.

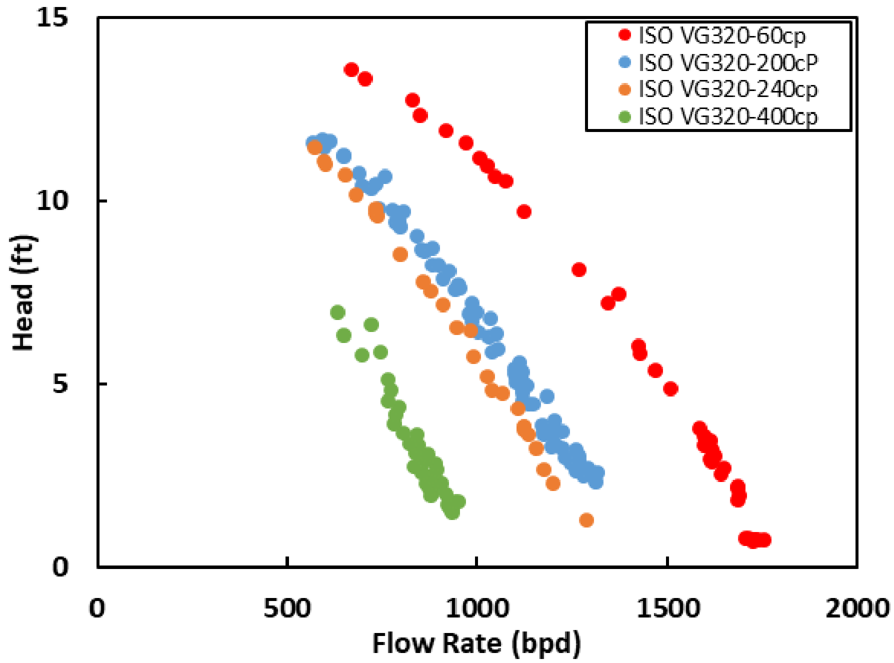

Figure 2.14 TE-2700 ESP Performance with ISO-VG320 Oil at 1,800 rpm

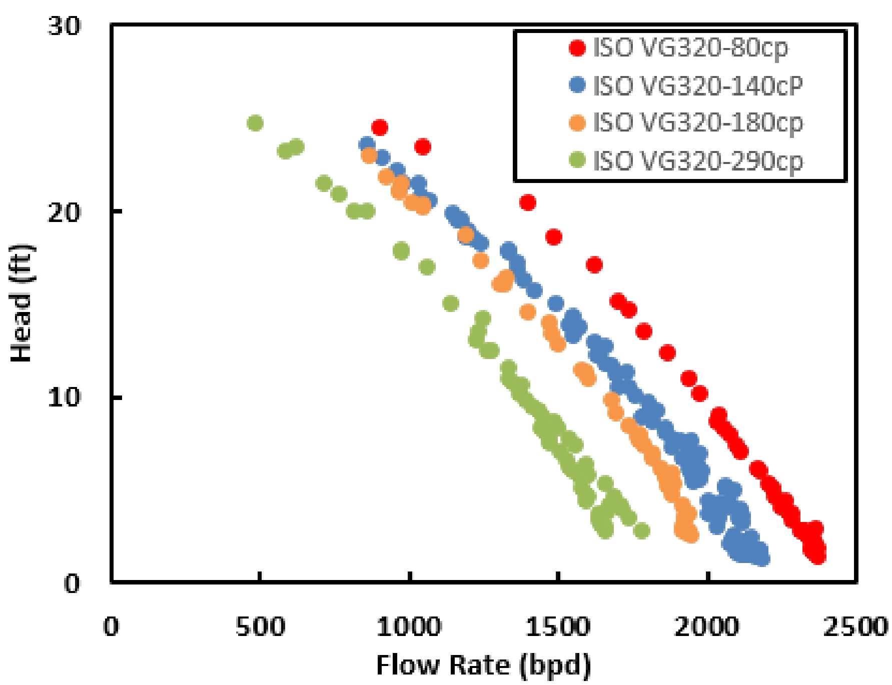

Figure 2.15 TE-2700 ESP Performance with ISO-VG320 Oil at 2,400 rpm

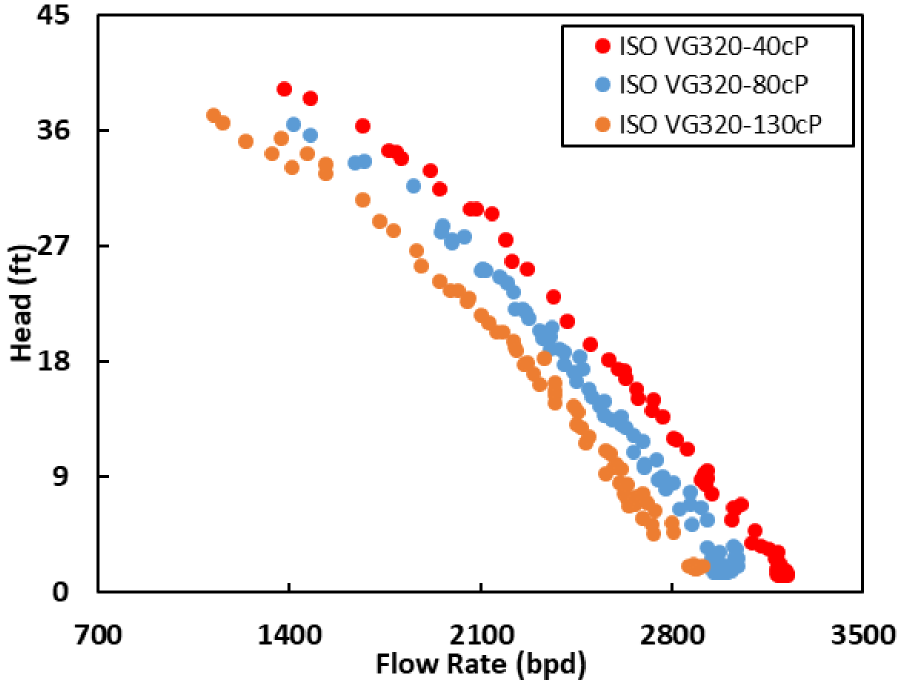

Figure 2.16 TE-2700 ESP Performance with ISO-VG320 Oil at 3,000 rpm

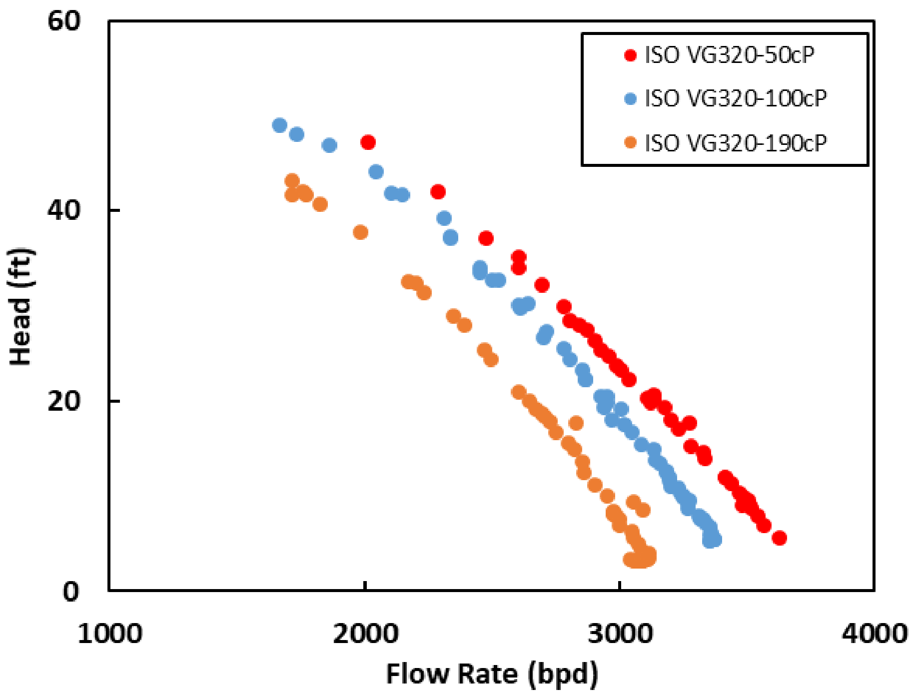

Figure 2.17 TE-2700 ESP Performance with ISO-VG320 Oil at 3,500 rpm

Figure 2.18 shows the comparison of pump head at different rotational speeds (1,800 rpm, 2,400 rpm, and 3,500 rpm) while the oil viscosities are similar (240 cP). Compared with high flow rates, head losses due to friction, turning, and recirculation at low flow rates are less significant. However, the head loss of an ESP becomes more significant at a higher flow rate.

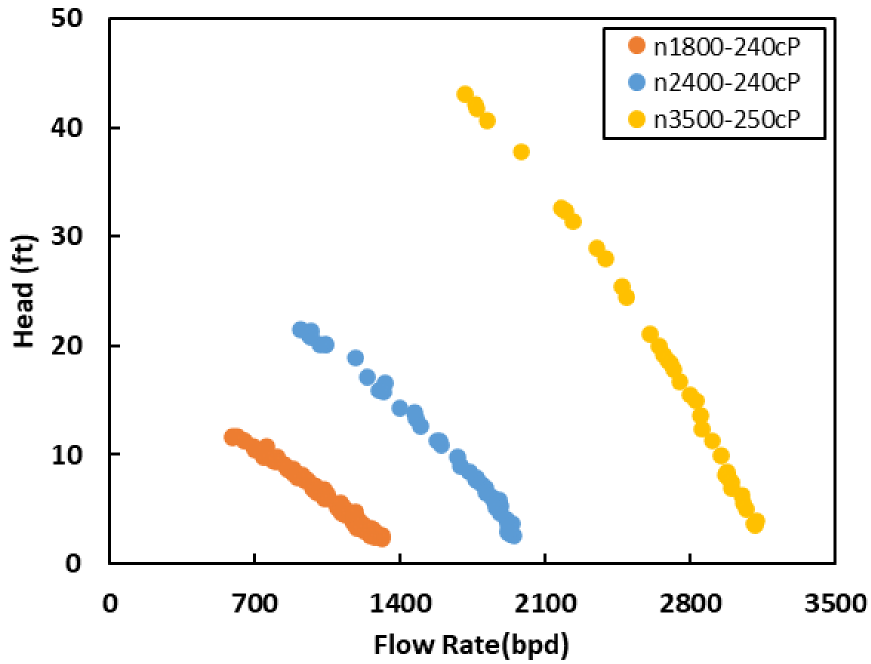

Figure 2.18 TE-2700 ESP Performance at Oil Viscosity≈240 cP

2.3.2 Oil-Water Emulsion Results

2.3.2.1 5% Water Cut Emulsion

The head curves of different viscosities at the rotational speed of 3,000 rpm are shown in Figure 2.19. The trends are similar to those of single-phase oil results.

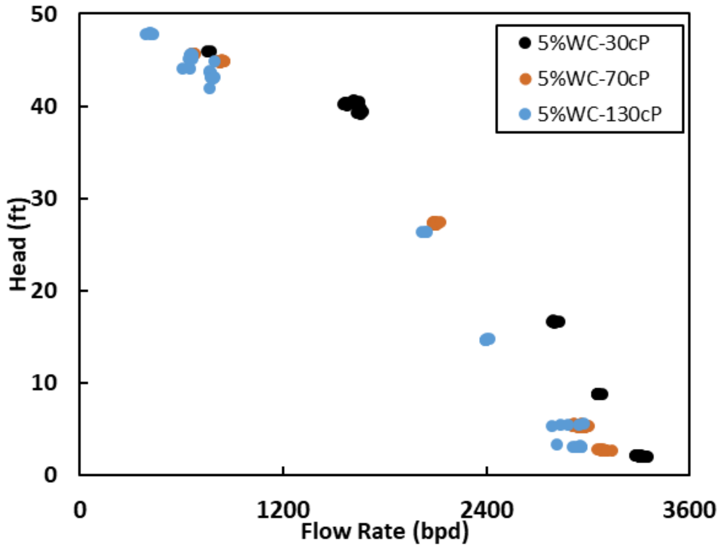

Figure 2.19 TE-2700 ESP Performance with 5% WC Emulsion at 3,000 rpm

2.4 Sampling

To calculate the oil and water fractions and measure working fluid viscosity, the oil sample was taken after each experiment. The sample was collected at the oil discharge port of the loop. A beaker was used to record the volume of the sample. Figure 2.20 (a) shows the pure ISO-VG320 oil sample, and Figure 2.20 (b) shows the 5% water cut emulsion sample. Small fractions from the emulsion sample were taken and observed under a microscope, as shown in Figure 2.21. The viscosity of the water-oil emulsion was measured the same way as explained in Section 2.3.1. The oil sample was stored until the gas bubbles ultimately came out from the oil. Then, the volume of the oil was checked to estimate the gas fraction. The water-oil emulsion sample was stored until oil and water were completed separated. Then, the water cut was checked to ensure it matched the designed fraction.

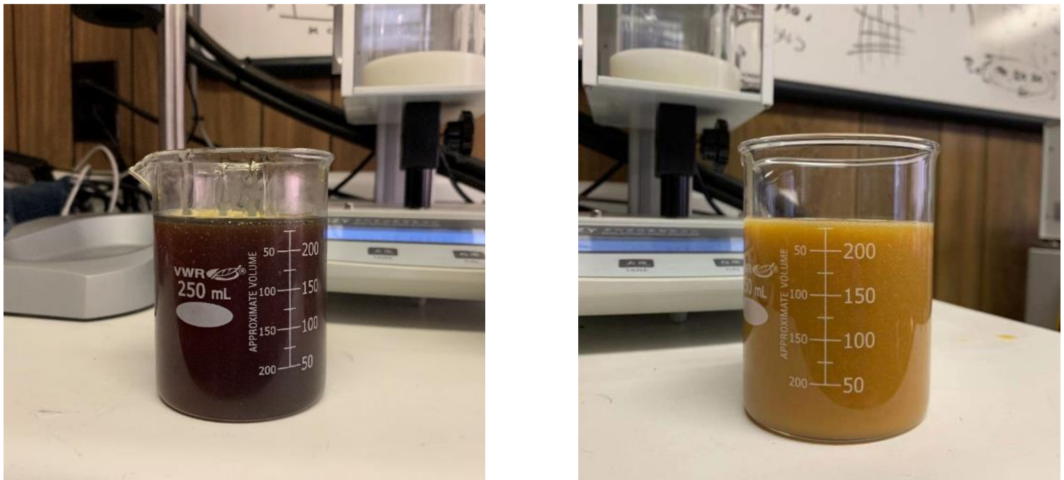

(a) (b)

Figure 2.20 Samples of Work Fluids (a) ISO-VG320 Oil (b) 5% Water/Oil Emulsion

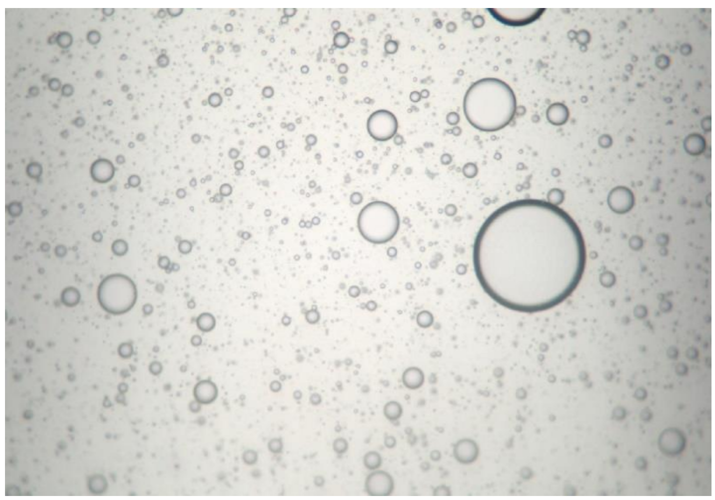

Figure 2.21 Water Droplets in ISO-VG320 Oil under Microscope

CHAPTER 3

ESP PERFORMANCE MODELING AND RESULTS

This chapter presents the modification of the TUALP mechanistic ESP performance prediction model for viscous and emulsion fluids. The results were compared to the previous version and experimental data. The model was improved by considering the emulsion rheology as well as modifying the correlation factors for friction and the theoretical head.

3.1 Emulsion Rheology Model

According to Kokal (2005), emulsion rheology is determined by densities, viscosities, volume fraction and interfacial tension of phases, droplet characteristics, and shear rate. The model was incorporated by Zhu et al. (2018e, 2019e, 2019f, 2019g) to predict ESP performance.

Since the continuous phase inversion point is essential to predict the effective viscosity, the water fraction corresponding to this point is determined using the Brinkman (1952) model:

$$\mu_E = \frac{\mu_C}{(1-\phi_D)^E} \tag{3.1}$$

where μ_C is continuous phase viscosity, ϕ_D is the volume fraction of the dispersed phase, and E is a modified exponent acquired from experiments. The water fraction at the inversion point can be expressed as:

$$\phi_W = \frac{1}{1+\tilde{\mu}^{1/E}} \tag{3.2}$$

where $\tilde{\mu} = \frac{\mu_O}{\mu_W}$.

The droplet size distribution has a tremendous influence on the rheology of the emulsion. Since the distribution is hard to be obtained, the Weber number is used to estimate the mean droplet diameter:

$$We = \frac{\rho_A v^2 l}{\sigma} \cong \frac{\rho_A Q^2}{\sigma V} \tag{3.3}$$

where ρ_A is the average density, Q is the flow rate, V is the pump channel volume of one stage, and σ is the interfacial tension obtained from experiments.

Turbulence effect is taken into consideration by introducing a representative Reynolds number:

$$Re = \frac{\rho_A v l}{\mu_A} \cong \frac{\rho_A Q}{\mu_A d} \tag{3.4}$$

where μ_A is the modeled emulsion viscosity, d is pump diameter.

Changing shear rate by changing pump rotational speed can lead to the change of effective viscosity of emulsion. The rotational speed is considered by using Strouhal number:

$$St \cong \frac{fV}{Q} \tag{3.5}$$

where f is the ESP rotational speed.

The final emulsion viscosity can be expressed with the factors above:

$$\mu_A = C(\mu_E - \mu_M) + \mu_M \tag{3.6}$$

where μ_M is the mixture base viscosity defined as:

$$\mu_M = \frac{\mu_W}{(1-\phi_O \phi_{OE})^E} \tag{3.7}$$

where $\phi_{OE} = 1 - \left(\frac{\mu_W}{\mu_O}\right)^{1/E}$.

C is a coefficient representing the effects of droplet size, turbulence, shear, and stage number in emulsion rheology:

$$C = \frac{(NWeRe)^n}{bSt^m} \tag{3.8}$$

where N is stage number from the ESP inlet. The exponents m and n need to be determined by experiments. According to Hattan (2018), the model can be extended to other types of pumps.

3.2 ESP Performance Model

The mechanistic model is developed based on Euler's equation for centrifugal pump. Head losses, including recirculation loss, friction loss, turn loss, leakage loss, diffuser loss, and disk loss, are considered (Zhu et al. 2019h, Zhu et al. 2019i). Although the previous model can predict ESP performance with high accuracy, special considerations on low flow rates, high viscosities, and low rotational speeds are still required to improve the model.

3.2.1 Euler's Equation for Centrifugal Pumps

Euler's Equation is applied to a two-dimensional system that filled with single-phase, incompressible ideal fluid. The velocities of the pump inlet and outlet are shown in Figure 3.1.

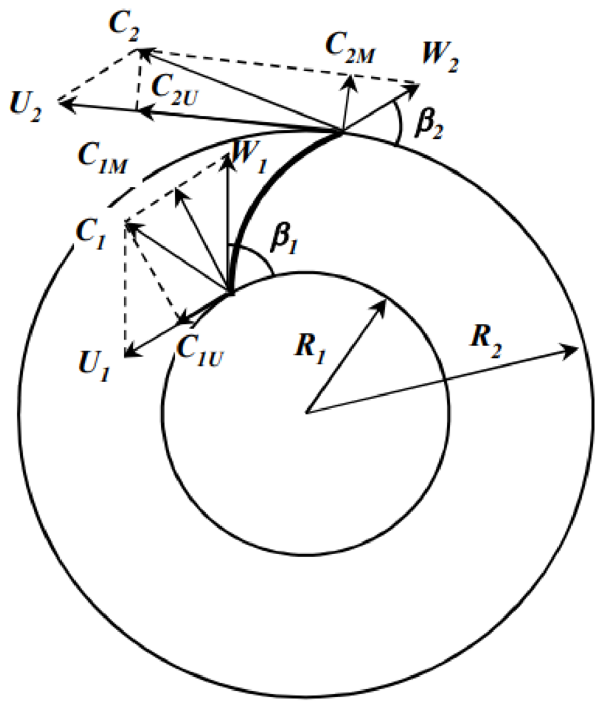

Figure 3.1 Velocity Triangles at Impeller Inlet and Outlet

The external torque acting on the impeller for the fluid to flow can be derived from Newton's second law of motion:

$$\tau = \dot{m}(R_2C_{2U} - R_1C_{1U}) \tag{3.9}$$

where R_1 is the radius of the inlet and R_2 is the radius of the outlet, C_{1U} is the fluid tangential velocity at the impeller inlet and C_{2U} is the fluid tangential velocity at the impeller outlet.

The tangential velocity of the impeller at the inlet and the outlet can be expressed as:

$$U_1 = R_1\Omega \tag{3.10}$$

$$U_2 = R_2\Omega \tag{3.11}$$

where Ω is the angular velocity of the impeller to be obtained from pump rotational speed, N:

$$\Omega = \frac{2\pi N}{60} \tag{3.12}$$

Then, the shaft power can be calculated by adopting the equations above as:

$$P_2 = \rho Q(U_2 C_{2U} - U_1 C_{1U}) \tag{3.13}$$

The hydraulic power, P_{hyd}, can be written as:

$$P_{hyd} = H_E \rho g Q \tag{3.14}$$

Assuming the flow has no losses, Equation (3.13) and Equation (3.14) are equivalent. Then, the Euler's Equation for the centrifugal pump can be expressed as:

$$H_E = \frac{U_2 C_{2U} - U_1 C_{1U}}{g} \tag{3.15}$$

Euler's head can also be rewritten based on the velocity trigonometry:

$$H_E = \frac{U_2^2 - U_1^2}{2g} + \frac{W_2^2 - W_1^2}{2g} + \frac{C_2^2 - C_1^2}{2g} \tag{3.16}$$

where the first term on the right side of Equation (3.16) is the static head as a result of centrifugal forces, the second term is the static head as a result of velocity change, and the third term is the dynamic head.

The fluid absolute velocity is defined as the meridional velocity. The meridional velocity at the impeller inlet is expressed as:

$$C_{1M} = \frac{Q + Q_{LK}}{(2\pi R_1 - Z_I T_B) y_{I1}} \tag{3.17}$$

where Q is the flow rate, Q_{LK} is the leakage flow rate, Z_I is the impeller blade number, T_B is the blade thickness projected to the radial direction, and y_{I1} is the impeller inlet height.

The meridional velocity at the impeller outlet is expressed as:

$$C_{2M} = \frac{Q + Q_{LK}}{(2\pi R_2 - Z_1 T_B) y_{I2}} \tag{3.18}$$

where y_{I2} is the impeller outlet height.

The relative velocity at the impeller inlet is expressed as:

$$W_1 = \frac{C_{1M}}{\sin\beta_1} \tag{3.19}$$

where β_1 is the blade angle from tangential at impeller inlet.

The relative velocity at the impeller outlet is expressed as:

$$W_2 = \frac{C_{2M}}{\sin\beta_2} \tag{3.20}$$

where β_2 is the blade angle from tangential at impeller outlet.

The fluid absolute velocity at the impeller inlet is then expressed as:

$$C_1 = \sqrt{C_{1M}^2 + \left(U_1 - \frac{C_{1M}}{\tan\beta_1}\right)^2} \tag{3.21}$$

The fluid absolute velocity at the impeller outlet is then expressed as:

$$C_2 = \sqrt{C_{2M}^2 + \left(U_2 - \frac{C_{2M}}{\tan\beta_2}\right)^2} \tag{3.22}$$

The fluid tangential velocity at the impeller inlet can be expressed as:

$$C_{1U} = U_1 - W_1 \cos\beta_1 \tag{3.23}$$

The fluid tangential velocity at the impeller outlet can be expressed as:

$$C_{2U} = U_2 - W_2 \cos\beta_2 \tag{3.24}$$

Equation (3.15) can be rewritten as:

$$H_E = \frac{U_2(U_2 - W_2\cos\beta_2) - U_1(U_1 - W_1\cos\beta_1)}{g} \tag{3.25}$$

Assuming no tangential fluid velocity at the impeller inlet, then $C_{1U} = 0$ and $C_1 = C_{1M}$, as shown in Figure 3.2. Euler's equation can be expressed as:

$$H_E = \frac{U_2^2}{g} - \frac{U_2 C_{2M}}{\tan\beta_2} \tag{3.26}$$

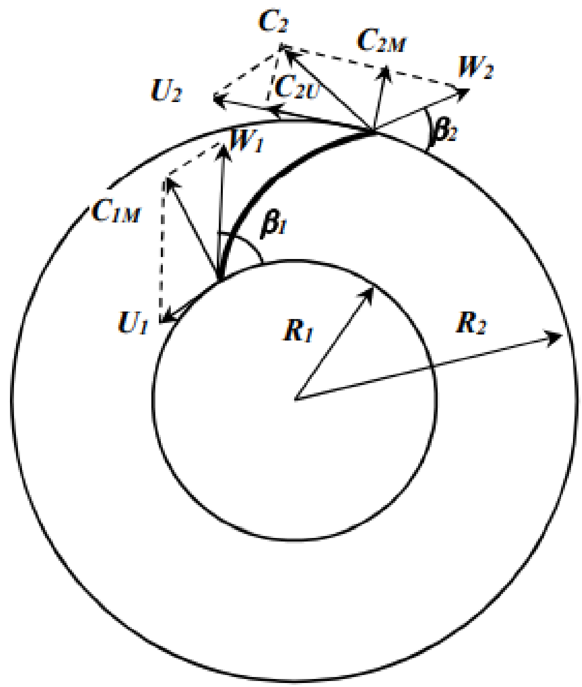

Figure 3.2 Velocity Triangles without Inlet Rotation

3.2.2 Effective Velocity at Impeller Outlet

When the direction of the fluid absolute velocity and the designated flow direction are the same, the BMP is reached. However, if mismatch happens, an effective velocity is introduced when the flowrate is different from the BMP flow rate (Zhu et al. 2019j, Zhu et al. 2019k). Figure 3.3 shows the velocity triangles when the flow rate is lower than that at the BMP.

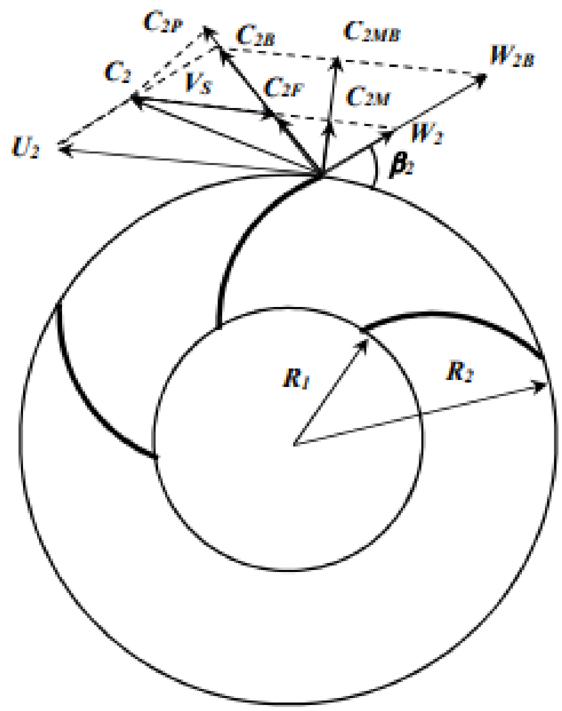

Figure 3.3 Velocity Triangles at Impeller Outlet for Q+Q_{LK}<Q_{BMP}

The fluid flow velocity at the impeller outlet is expressed as:

$$C_{2F} = C_{2B}\frac{Q}{Q_{BMP}} \tag{3.27}$$

where C_{2B} is the absolute fluid velocity at the impeller outlet at the BMP.

The shear velocity, if C_{2F} is higher than C_2, can be expressed as:

$$V_S = U_2\frac{Q_{BMP}-(Q+Q_{LK})}{Q_{BMP}} \tag{3.28}$$

The projected velocity, C_{2P}, can be derived as:

$$C_{2P} = \frac{C_2^2+C_{2F}^2-V_S^2}{2C_{2F}^2} \tag{3.29}$$

Fluid circulation takes place in the impeller because of the shear effects, as shown in Figure 3.4. As a result, the kinetic energy is not fully converted to static pressure. Shear velocity, impeller channel size, and fluid viscosity are the dominant factors for recirculation flow. Therefore, the

Reynolds number is introduced to estimate the recirculation head loss:

$$Re_C = \frac{\rho V_S D_C}{\mu} \tag{3.30}$$

where D_C is the representative impeller channel width at the outlet, and can be calculated:

$$D_C = \frac{2\pi R_2}{Z_I}\sin\beta_2 - T_B \tag{3.31}$$

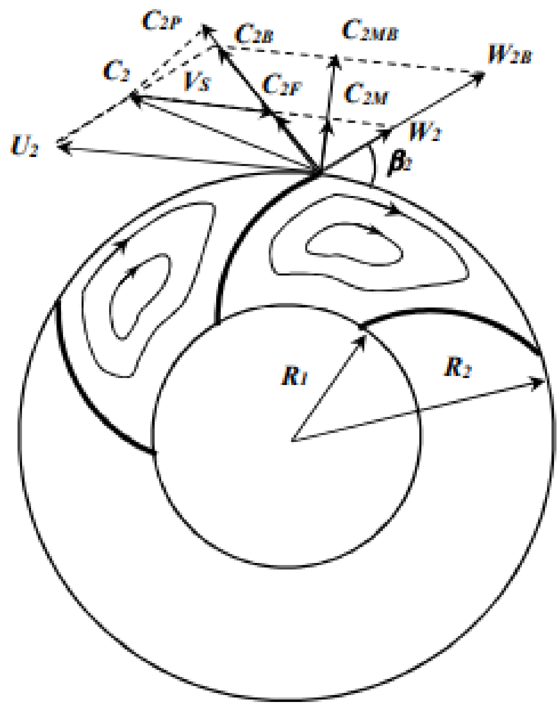

Figure 3.4 Recirculation Effect in Impeller

A correlation developed from experimental data is expressed as:

$$C_{2E} = C_{2F} + \sigma(C_{2P} - C_{2F}) \tag{3.32}$$

where σ is the velocity reduction factor, which can also be named the slip factor:

$$\sigma = \frac{\left(\frac{\mu_W}{\mu_O}\right)^{0.1}}{1+0.02Re_C^{0.2}} \tag{3.33}$$

If the pump in-situ flow rate is higher than that at the BMP, as shown in Figure 3.5, the shear velocity can be expressed as:

$$V_S = U_2 \frac{(Q+Q_{LK})-Q_{BMP}}{Q_{BMP}} \tag{3.34}$$

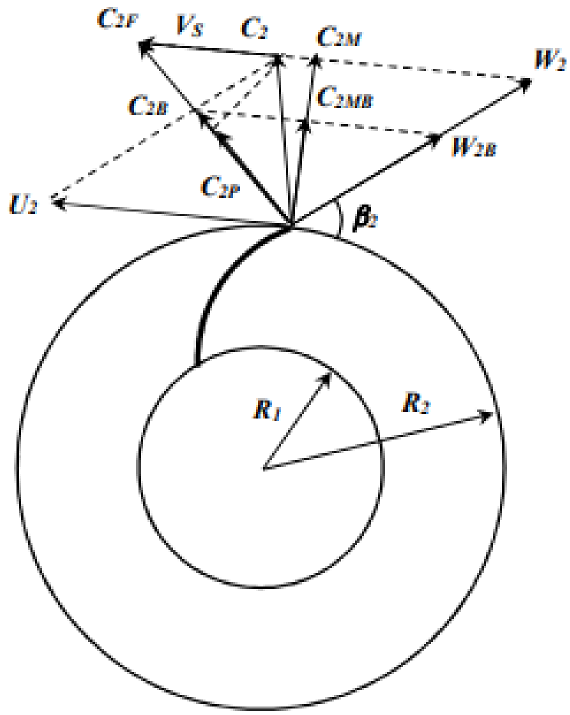

Figure 3.5 Velocity Triangles at Impeller Outlet for Q+Q_{LK}>Q_{BMP}

The effective velocity, C_{2E}, is now expressed as:

$$C_{2E} = \frac{C_2^2+C_{2F}^2-V_S^2}{2C_{2F}^2} \tag{3.35}$$

The effective Euler head thus can be expressed as:

$$H_{EE} = H_E + \frac{C_{2E}^2-C_2^2}{2g} \tag{3.36}$$

3.2.3 Head Losses

3.2.3.1 Recirculation Loss

Based on the derivations of Equation (3.36), the recirculation head loss can be expressed as:

$$h_{recirculation} = \frac{C_2^2 - C_{2E}^2}{2g} \tag{3.37}$$

3.2.3.2 Friction Loss

The previous model treated the fluid inside the impeller and the diffuser as channel flow without considering other factors that contribute to the friction loss. Only Churchill (1977) equations, which is developed for circular, straight, stationary pipe, are used to calculate the friction factor:

The Churchill equation for the friction factor can be expressed as:

$$f = 8\left[\left(\frac{8}{Re}\right)^{12} + \frac{1}{(A+B)^{1.5}}\right]^{1/12} \tag{3.38}$$

where A and B can be expressed as:

$$A = \left[2.457 \ln\left(\frac{1}{\left(\frac{7}{Re}\right)^{0.9} + 0.27\frac{\varepsilon}{D}}\right)\right]^{16} \tag{3.39}$$

$$B = \left(\frac{37{,}530}{Re}\right)^{16} \tag{3.40}$$

The Reynolds number can be expressed as:

$$Re = \frac{d_H Q_L \rho_L}{2\pi r \mu_L \sin\beta} \tag{3.41}$$

Sun and Prado (2003) proposed a correlation of friction factor in rotating ESPs. In ESP, the friction factor needs to consider the cross-section shape effect (F_γ), the pipe curvature effect (F_β), and the rotational speed effect (F_ω). The cross-section shape effect (F_γ) is expressed as:

$$F_\gamma = \left[\frac{2}{3} + \frac{11}{24} l_L (2 - l_L)\right]^{-1} \qquad Re \leq 2300$$

(3.42)

$$F_\gamma = \left[\frac{2}{3} + \frac{11}{24} l_L (2 - l_L)\right]^{-0.25} \qquad Re > 2300$$

(3.43)

where l_L is the aspect ratio of the rectangular cross-section for liquid defined as:

$$l_L = \frac{min(a_L, b_L)}{max(a_L, b_L)} \tag{3.44}$$

where a_L is the channel width, and b_L is the channel height for the impeller or diffuser.

The critical Reynolds number is introduced to take care of the pipe curvature effect as:

$$N_{Re} = 2 \times 10^4 \times \left(\frac{R_c}{r_H}\right)^{-0.32} \qquad \frac{R_c}{r_H} < 860$$

(3.45)

$$N_{Re} = 2300 \qquad \frac{R_c}{r_H} \geq 860$$

(3.46)

where R_c is the radius of curvature along a channel, r_H is the hydraulic radius based on the hydraulic diameter:

$$R_c = \frac{1}{\sin\beta} \frac{1}{-\frac{d\beta(r)}{dr} + \frac{1}{r \tan\beta}} \tag{3.47}$$

$$r_H = \frac{d_H}{2} \tag{3.48}$$

The pipe curvature effect can then be concluded as:

For laminar effect ($Re < N_{Re}$)

$$F_\beta = 0.266\,\mathrm{Re}^{0.389}\left(\frac{R_c}{r_H}\right)^{-0.1945} \tag{3.49}$$

For turbulent effect ($Re > N_{Re}$)

$$F_\beta = \begin{cases} \left(\mathrm{Re}\left(\frac{R_c}{r_H}\right)^{-2}\right)^{0.05} & \mathrm{Re}\left(\frac{R_c}{r_H}\right)^{-2} \geq 300 \\ 0.092\left(\mathrm{Re}\left(\frac{R_c}{r_H}\right)^{-2}\right)^{0.25} + 0.962 & 300 \geq \mathrm{Re}\left(\frac{R_c}{r_H}\right)^{-2} > 0.034 \\ 1 & \mathrm{Re}\left(\frac{R_c}{r_H}\right)^{-2} \leq 0.034 \end{cases} \tag{3.50}$$

The rotational Reynolds number, Re_ω, is introduced to take care of the rotational speed effect defined by:

$$Re_\omega = \frac{\omega d_H^2 \rho_l}{\mu_l} \tag{3.51}$$

The rotational speed effect, F_ω, can then be expressed as:

$$F_\beta = \begin{cases} 1 & \frac{Re_\omega^2}{Re} < 1 \\ 0.942 + 0.058\left(\frac{Re_\omega^2}{Re}\right)^{0.282} & 1 < \frac{Re_\omega^2}{Re} < 15 \\ 0.942\left(\frac{Re_\omega^2}{Re}\right)^{0.05} & \frac{Re_\omega^2}{Re} > 15 \end{cases} \tag{3.52}$$

Thus, the friction factor is calculated as:

$$f_{\gamma\beta\omega} = F_\gamma F_\beta F_\omega f \tag{3.53}$$

The friction loss can then be calculated by:

$$h_{friction} = \frac{f_{\gamma\beta\omega} Q^2}{8 g D_H \pi^2 b_m^2 sin^3 \beta_m} \frac{r_2 - r_1}{r_1 r_2} \tag{3.54}$$

3.2.3.3 Turn Loss

Turning loss takes place when the fluid flow direction changes through the impeller and diffuser. The turning head loss in the impeller can be expressed as:

$$H_{TI} = f_{TI}\frac{V_I^2}{2g} \tag{3.55}$$

The turning head loss in the diffuser can be expressed as:

$$H_{TD} = f_{TD}\frac{V_D^2}{2g} \tag{3.56}$$

where f_{TI} and f_{TD} are the local drag coefficients based on experimental data.

Then, the total turning loss can be expressed as:

$$h_{shock} = f_{TI}\frac{V_I^2}{2g} + f_{TD}\frac{V_D^2}{2g} \tag{3.57}$$

3.2.3.4 Leakage Loss

In an ESP, the reverse flow goes through the secondary leakage flow passage, including balance holes and the clearance between the impeller and the diffuser, as shown in Figure 3.6. The leakage geometries in an ESP stage is shown in Figure 3.7.

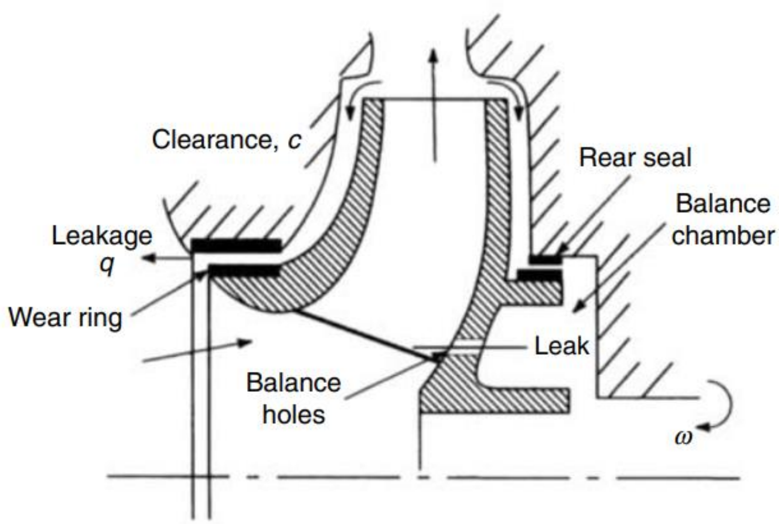

Figure 3.6 Balancing of Axial Thrust (Tuzson 2000)

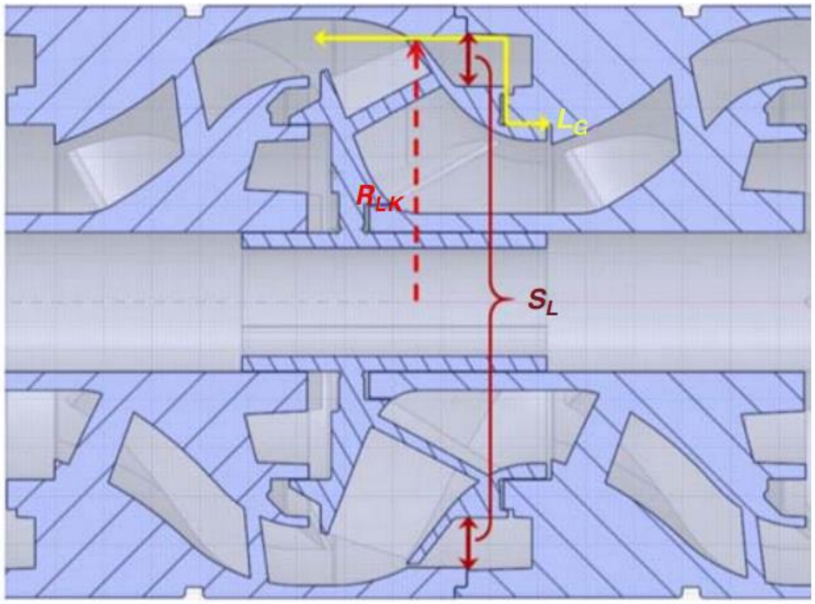

Figure 3.7 Leakage Geometries in an ESP Stage

The head loss through the leakage passage can be expressed as:

$$h_{leakage} = H_{IO} - \frac{U_2^2 - U_{LK}^2}{8g} \quad (3.58)$$

where H_{IO} is the head increase across the impeller, U_{LK} is the tangential velocity due to the impeller rotation at the leakage. The head increase across the impeller can be calculated as:

$$H_{IO} = H_{EE} - H_{FI} - H_{TI} \quad (3.59)$$

The tangential velocity due to the impeller rotation at the leakage is:

$$U_{LK} = R_{LK}\Omega \quad (3.60)$$

where R_{LK} is the radius of the leakage clearance.

As shown in Figure 3.7, the secondary flow passage is complicated. Therefore, friction, sudden expansion, and sudden contraction are considered to obtain the total head loss through the leakage area:

$$h_{leakage} = f_{CON}\frac{V_L^2}{2g} + f_{EXP}\frac{V_L^2}{2g} + f_{LK}\frac{V_L^2 L_G}{2gS_I} \tag{3.61}$$

where L_G is the leakage channel length, S_I is the leakage width, and f_{CON} and f_{EXP} are the local hydraulic loss factors due to contraction and expansion. A $f_{CON} = 0.5$ and $f_{EXP} = 1.0$ are used.

$$V_L = \sqrt{\frac{2gh_{leakage}}{f_{LK}\frac{L_G}{S_I}+1.5}} \tag{3.62}$$

Then, the leakage flow rate,

$$Q_{Lk} = 2\pi R_{LK} S_L V_L \tag{3.63}$$

3.2.4 Correction Factors for Theoretical Head

The slip factor, δ_s, is introduced to recalculate the theoretical pump head H_{th} to investigate the mismatch between the real outflow velocity and the designed outflow velocity. The Euler head with pre-rotation can be written as

$$H_E = \frac{\Omega^2 r_2^2}{g} - \frac{Q\Omega}{2\pi g h \tan\beta_2}, \tag{3.64}$$

where δ_s in the previous model is proposed by Wiesner (1967) as

$$\delta_s = 1 - \frac{\sqrt{\sin\beta_2}}{(Z_I)^{0.7}}, \tag{3.65}$$

δ_s in this study is modified by Zhang (2017) as:

$$\delta_s = 1 - \frac{\sqrt{\sin\beta_2}}{(Z_I)^{1.5\left(\frac{N_{S,ref}}{N_S}\right)^{0.4}}}, \tag{3.66}$$

where $N_{S,ref}$ is the reference specific speed.

The theoretical head H_{th} can then be calculated as

$$H_{th} = \delta_s \frac{\Omega^2 r_2^2}{g} - \frac{Q\Omega}{2\pi g h \tan\beta_2} \tag{3.67}$$

3.3 Mechanistic Model Setup

With all the losses determined, the mechanistic model of ESP performance prediction can be established following the flow chart, as shown below.

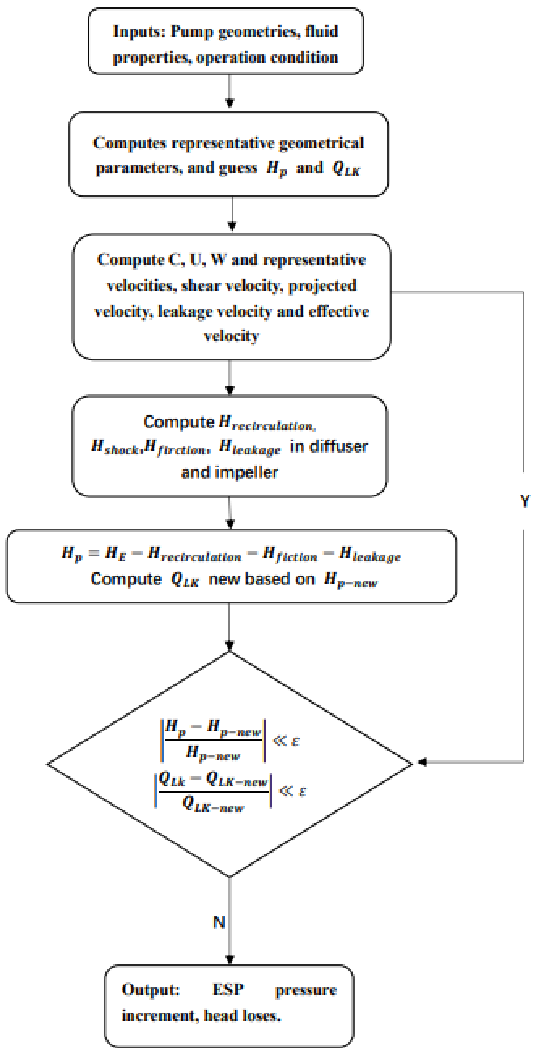

Figure 3.8 Flow Chart of Modified Mechanistic Model

The model is coded in Python in order to obtain a better prediction efficiency with a much less calculation time. The fluid properties, pump geometries, and operating conditions are input into the code as parameters for the calculations of the model. The pump geometries are shown in Table 3.1.

Table 3.1 TE-2700 ESP Specifications

ESP	**Component**	**Value**
Impeller	Blade Number	5
	Tangential Blade angle at Inlet (°)	19.5
	Tangential Blade angle at Outlet (°)	24.7
	Blade Thickness (mm)	2.72
	Channel Length (mm)	76.0
	Inlet Channel Height (mm)	12.2
	Outlet Channel Height (mm)	7.84
	Inlet Radius (mm)	17.5
	Outlet Radius (mm)	56.1
Diffuser	Vane Number	9
	Channel Length (mm)	87.1
	Partition Wall Thickness (mm)	4.48
	Inlet Radius (mm)	54.7
	Outlet Radius (mm)	22.0

The model is compared with the catalog curve provided by the manufacturer at 3,500 rpm and 3,000 rpm. As shown in Figure 3.9 and Figure 3.10, the error between the predicted results and the catalog curve is less than 10%.

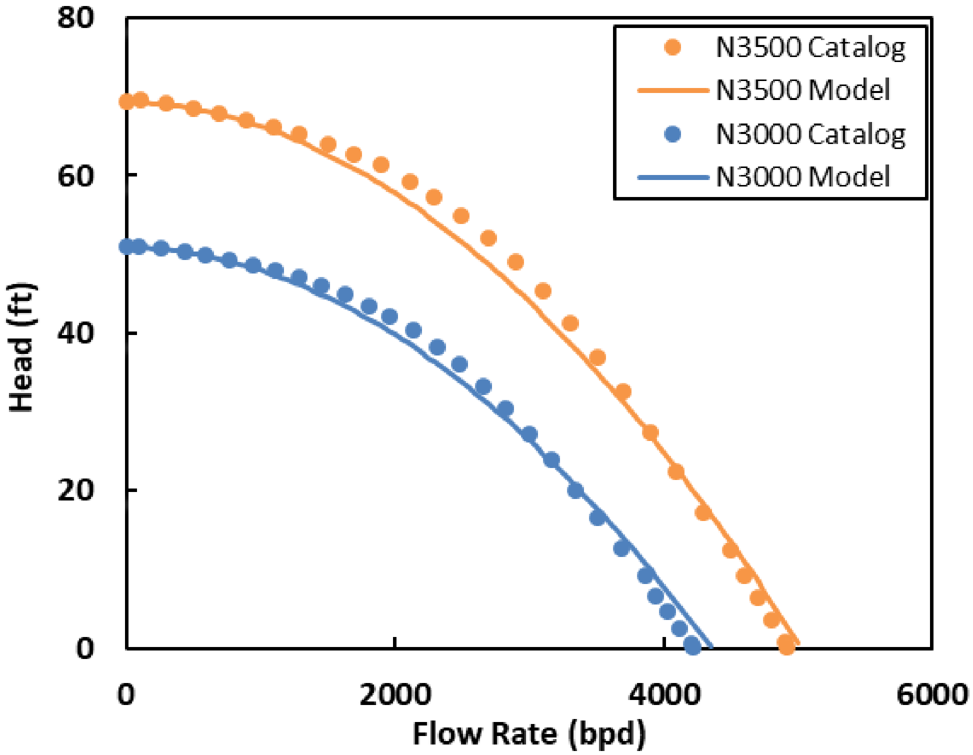

Figure 3.9 Comparison between Modified Model and Catalog

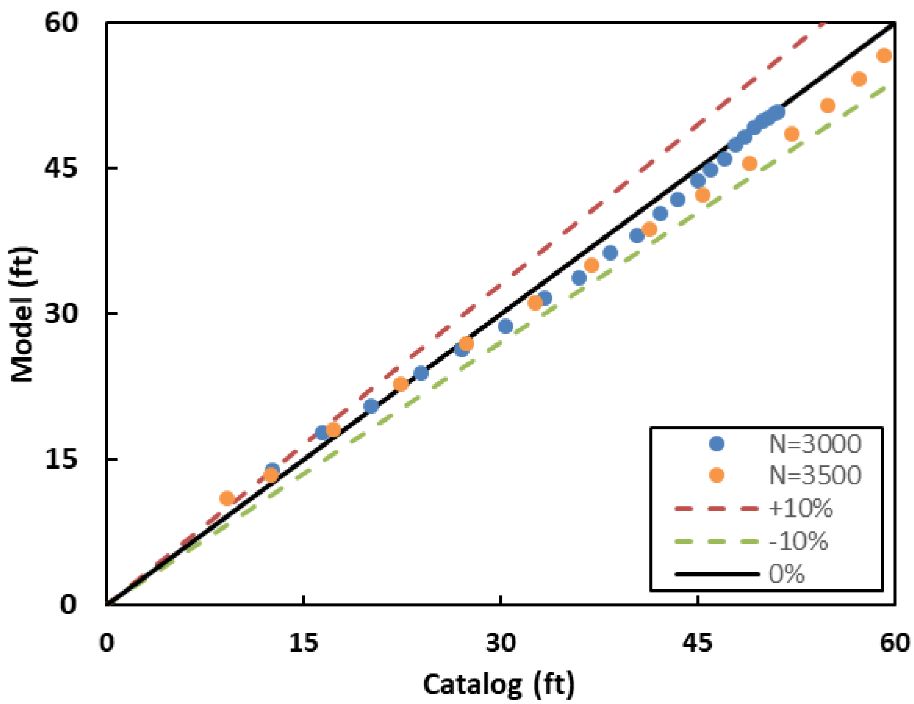

Figure 3.10 Error between the Predicted Results and Catalog Curve

3.4 Mechanistic Model Validation

In this section, the mechanistic model is validated by experimental data of TE-2700 with a broad range of viscosity at the rotational speed of 1,800 rpm, 2,400 rpm, 3,000 rpm, and 3,500 rpm as shown in Figure 3.11 to Figure 3.14. The improvement of the modified model, which adopts new correlation factors, is analyzed by comparing it with the previous model predictions. The validation covers viscosities ranging from 1 to 400 cP, and the results agree well with the experimental tests. Figure 3.15 is the comparison between experimental data and model predictions for the oil-water emulsion with a water cut of 5%. The emulsion is treated as a single-phase liquid, with the volumetric average density of oil and water. The results match the model in general.

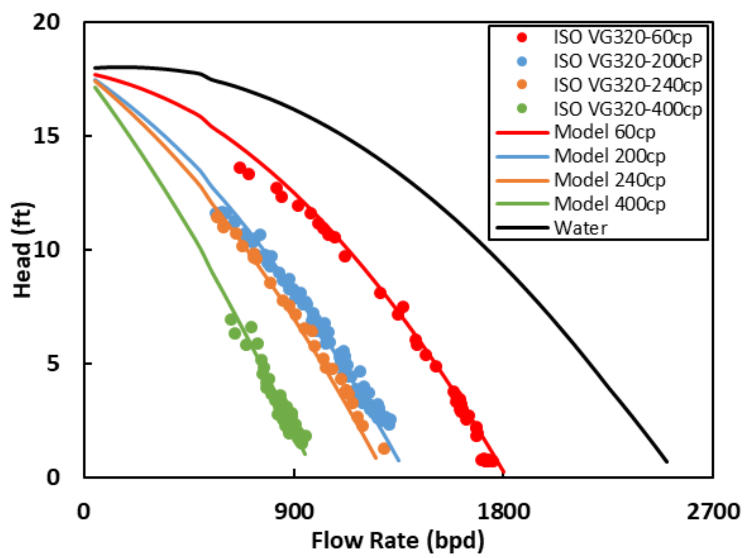

Figure 3.11 TE-2700 ESP Comparison of Modified Model and Experimental Data at 1,800 rpm

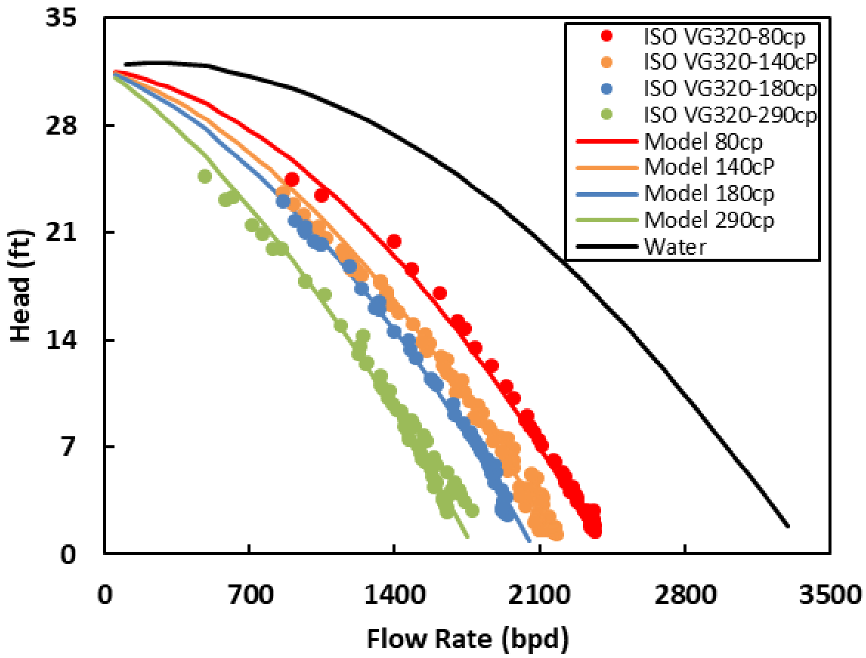

Figure 3.12 TE-2700 ESP Comparison of Modified Model and Experimental Data at 2,400 rpm

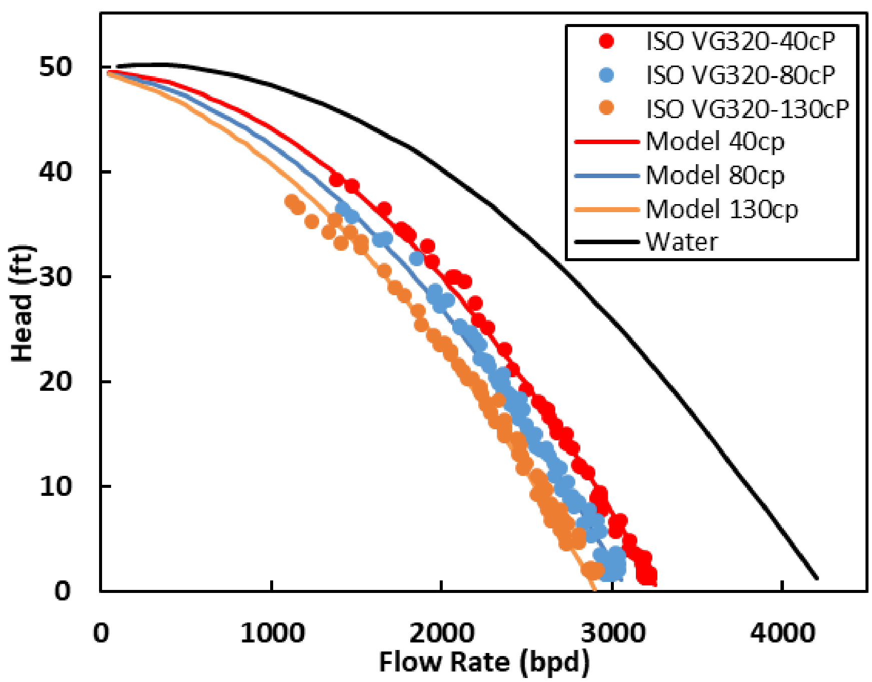

Figure 3.13 TE-2700 ESP Comparison of Modified Model and Experimental Data at 3,000 rpm

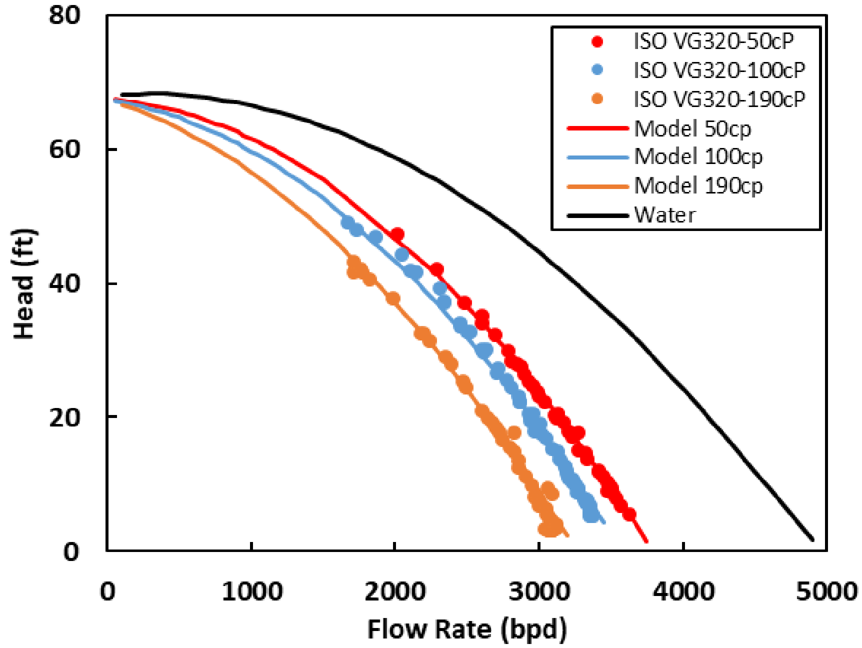

Figure 3.14 TE-2700 ESP Comparison of Modified Model and Experimental Data at 3,500 rpm

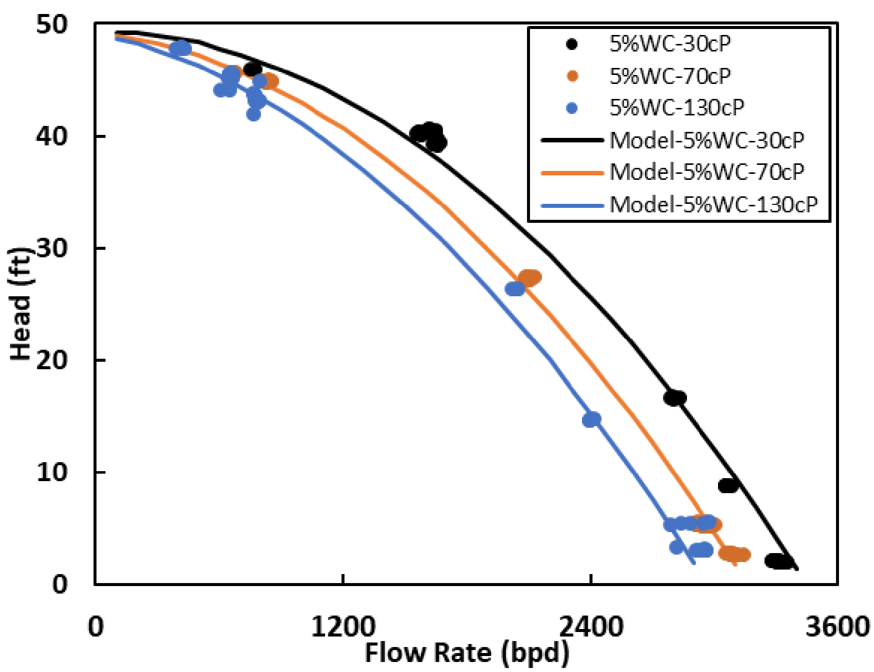

Figure 3.15 TE-2700 ESP Comparison of Modified Model and Experimental Data at 3,000 rpm for 5% WC Emulsion

The new model is compared with the previous version against the experimental data, as shown in Figure 3.16 to Figure 3.18. Both models can predict the pump head with high accuracy.

Compared with the previous version, the improved model is more accurate at lower flow rates.

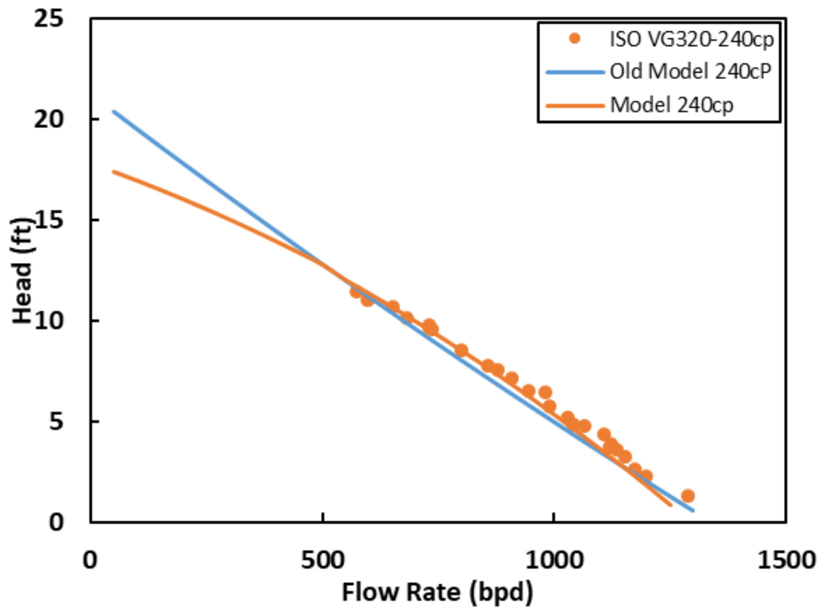

Figure 3.16 TE-2700 ESP Comparison of Modified Model and Previous Version against Experiment Data at 1,800 rpm

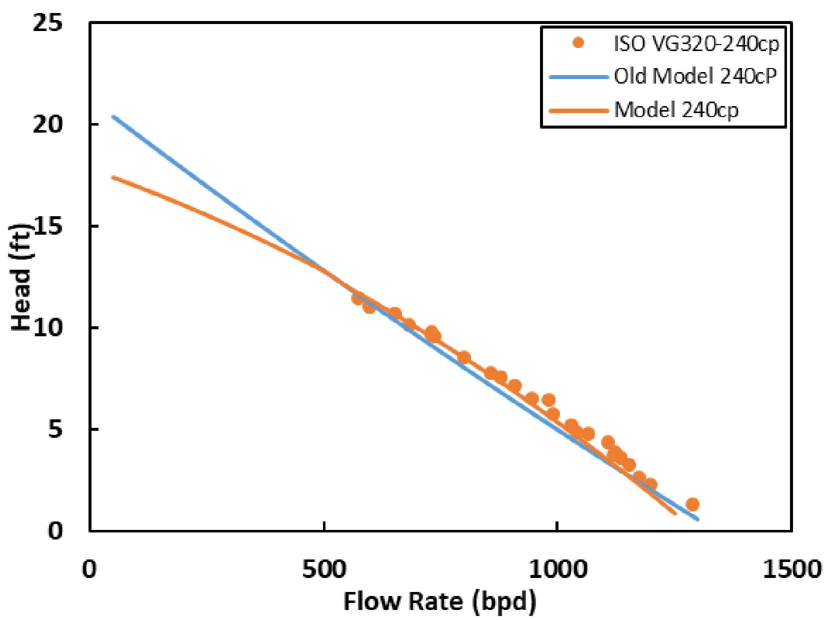

Figure 3.17 TE-2700 ESP Comparison of Modified Model and Previous Version against Experiment Data at 2,400 rpm

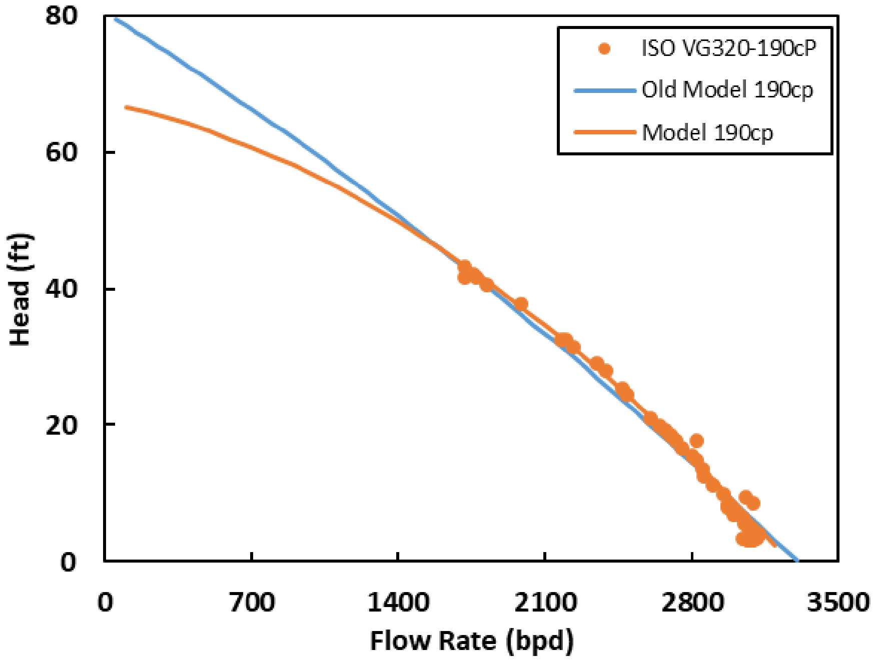

Figure 3.18 TE-2700 ESP Comparison of Modified Model and Previous Version against Experiment Data at 3,500 rpm

CHAPTER 4

CONCLUSIONS AND RECOMMENDATIONS

The fluid viscosity effect and emulsions effect on ESP performance are investigated experimentally and modeled mechanistically in this study. The main conclusions and recommendations are summarized below.

4.1 Conclusions

4.1.1 Experimental Study

1. The reliability of the experimental setup in this study was validated by comparisons with the catalog curve and the previous experimental data collected by Zhang (2017).
2. The TE-2700 ESP was tested with ISO VG320 oil at rotational speeds of 1800, 2400, 3000, and 3500 rpm. The test oil viscosities are 60 to 400 cP at 1800 rpm, 80 to 290 cP at 2400 rpm, 40 to 130 cP at 3000 rpm, and 50 to 190 cP at 3500 rpm.
3. The fluid viscosity is affected by loop temperature, and the viscosity-temperature relationship is measured using a rotational viscometer with collected samples.
4. Pump head decreases with the increase of oil viscosity, which is caused by higher energy loss due to increased shear stress.

5. The relationship between the pump head and flow rate becomes more linear at high fluid viscosity than that of low fluid viscosity.

4.1.2 Mechanistic Modeling

1. The previous TUALP ESP mechanistic model has been improved by replacing the friction head loss correlation and theoretical head correlation. Cross-section shape effect (F_{γ}), the pipe curvature effect (F_{β}), and the rotational speed effect (F_{ω}) are included in the new friction correlation. A new slip factor correlation is added to calculate the theoretical head.
2. The hydraulic pressure increase predicted by the new mechanistic model with water as the working fluid agrees well with the catalog curve.
3. The old mechanistic model and the new mechanistic model are compared against experimental data at different rotational speeds. Compared with the prediction of the previous model, the modified model matches the experimental data and trend better at a lower flow rate.

4.2 Recommendations

The following suggestions are made for the future ESP high viscosity and water-oil emulsion test and modeling:

1. Oil with higher viscosity can be tested to validate the proposed mechanistic model in the broader viscosity range.
2. The torque sensor needs to be replaced to obtain accurate torque and efficiency curve.

3. At the beginning of the test, gas may be carried by working fluid. Therefore, the liquid input port should be extended to ensure that gas will be separated in this section.
4. The pipe-in-pipe heat exchanger needs to be improved to maintain the loop temperature better.

NOMENCLATURE

BEP	best efficiency point
BMP	best match point
DAQ	data acquisition system
ESP	electrical submersible pump
PV	pipe viscometer
VSD	variable speed drive
A_{SD}	diffuser channel total wall area, L^2, m^2
A_{SI}	impeller channel total wall area, L^2, m^2
C_1	absolute fluid velocity at impeller inlet, L/T, m/s
C_{1M}	meridional velocity at impeller inlet, L/T, m/s
C_{1U}	fluid tangential velocity at impeller inlet, L/T, m/s
C_2	absolute fluid velocity at impeller outlet, L/T, m/s
C_{2B}	absolute fluid velocity at impeller outlet corresponding to BMP, L/T, m/s
C_{2E}	effective velocity at impeller outlet, L/T, m/s
C_{2F}	fluid velocity outside impeller, L/T, m/s
C_{2M}	meridional velocity at impeller outlet, L/T, m/s
C_{2P}	projected velocity, L/T, m/s

C_{2U}	fluid tangential velocity at impeller outlet, L/T, m/s
C_D	drag coefficient
C_H	head correction factor
C_q	flowrate correction factor
C_η	efficiency correction factor
$\overline{d}$	average droplet sizes, L, m
d	impeller diameter, L, m
D_C	representative impeller channel width at outlet, L, m
D_D	diffuser representative (hydraulic) diameter, L, m
D_I	impeller representative (hydraulic) diameter, L, m
D_L	leakage diameter, L, m
dP	differential pressure, M/(LT^2), Pa
f	friction factor
f_{FD}	friction factor in diffuser
f_{FI}	friction factor in impeller
f_{LK}	leakage friction factor
f_{TD}	local drag coefficient in diffuser
f_{TI}	local drag coefficient in impeller
F_γ	cross-section shape effect
F_β	pipe curvature effect
F_ω	rotational speed effect

h	channel height, L, m
H	pump head, L, m
H_{BEP}	head at BEP, L, m
H_E	Euler's head, L, m
H_{EE}	effective Euler's head, L, m
H_{FD}	head loss due to friction in diffuser, L, m
H_{FI}	head loss due to friction in impeller, L, m
H_{IO}	head increase across impeller, L, m
H_{LK}	pressure head difference across leakage, L, m
H_{oil}	pump head with oil, L, m
H_{TD}	head loss due to turn in diffuser, L, m
H_{TI}	head loss due to turn in impeller, L, m
H_{vis}	pump head with viscous fluid, L, m
H_{water}	pump head with water, L, m
L_D	diffuser channel length, L, m
L_{LK}	leakage channel length, L, m
L_I	impeller channel length, L, m
N	rotational speed, 1/T, rpm
N_s	specific speed
P	pressure, $M/(LT^2)$, Pa
P_2	shaft power, ML^2/T^3, $kg{\cdot}m^2/s^3$

P_{hyd}	hydraulic power, ML^2/T^3, $kg \cdot m^2/s^3$
Q	volumetric flowrate, L^3/T, m^3/s
q_{BEP}	flowrate at BEP, L^3/T, m^3/s
Q_{BMP}	volumetric flowrate at BMP, L^3/T, m^3/s
Q_{LK}	leakage volumetric flowrate, L^3/T, m^3/s
q_{vis}	viscous fluid flowrate, L^3/T, m^3/s
q_{water}	water flowrate, L^3/T, m^3/s
R_1	radius of impeller inlet, L, m
R_2	radius of impeller outlet, L, m
R_D	Reynolds number by Ippen
Re	Reynolds number
Re_C	recirculation effect Reynolds number
Re_D	Reynolds numbers in diffuser
Re_I	Reynolds numbers in impeller
Re_L	leakage Reynolds number
$Re_{Stepanoff}$	Reynolds number by Stepanoff
R_{LK}	radius corresponding to leakage, L, m
S_L	leakage width, L, m
St	Strouhal number
t	time, T, s
T	temperature, ℃

T	blade thickness, L, m
U_1	impeller tangential velocity at inlet, L/T, m/s
U_2	impeller tangential velocity at outlet, L/T, m/s
U_{LK}	tangential velocity due to impeller rotation at leakage, L/T, m/s
v	velocity, L/T, m/s
V	volume, L^3, m^3
V_D	representative fluid velocity in diffuser, L/T, m/s
V_I	representative fluid velocity in impeller, L/T, m/s
V_L	fluid velocity at leakage, L/T, m/s
Vol_D	diffuser channel volume, L^3, m^3
Vol_I	impeller channel volume, L^3, m^3
V_S	shear velocity, L/T, m/s
W_1	relative velocity with respect to impeller at inlet, L/T, m/s
W_2	relative velocity with respect to impeller at outlet, L/T, m/s
We	Weber number
y_{I1}	impeller inlet height, L, m
y_{I2}	impeller outlet height, L, m
Z_I	impeller blade number

Greek Symbols

η	efficiency

μ	dynamic viscosity, M/(LT), Pa·s
μ_{eff}	effective viscosity, M/(LT), Pa·s
β_1	blade angle from tangential at impeller inlet, °
β_2	blade angle from tangential at impeller outlet, °
η_{vis}	efficiency with viscous fluid
η_{water}	efficiency with water
ν	kinematic viscosity, L^2/T, m^2/s
ρ	density, M/L^3, kg/m^3
σ_s	slip factor
ω	angular velocity, 1/T, 1/s
Ω	angular speed, L/T, m/s
φ	flow coefficient
ψ	head coefficient

BIBLIOGRAPHY

1. Amaral, G., Estevam, V., Franca, F.A., 2009. On the Influence of Viscosity on ESP Performance. *SPE Production & Operations*. 24(2): 303-310.

2. Amaral, G.D.L., 2007. Single-phase Flow Modeling of an ESP Operating with Viscous Fluids. MSc Thesis, State University of Campinas, Campinas, São Paulo, Brazil.

3. Banjar, H., 2012. Experimental Study of Liquid Viscosity Effect on Two-Phase Stage Performance of Electric Submersible Pumps. MSc Thesis. The University of Tulsa.

4. Banjar, H., 2018. Experiments, CFD Simulation, and Modeling of Oil Viscosity and Emulsion Effects on ESP Performance. Ph.D. Dissertation. The University of Tulsa

5. Banjar, H.M., Gamboa, J., Zhang, H.-Q., 2013. Experimental Study of Liquid Viscosity Effect on Two-phase Stage Performance of Electrical Submersible Pumps. Proceedings of SPE Annual Technical Conference and Exhibition, New Orleans, Louisiana.

6. Barrios, L.J., Scott, S.L., Rivera, R., and Sheth, K.K., 2012. ESP Technology Maturation: Subsea Boosting System with High GOR and Viscous Fluid. doi:10.2118/159186-MS

7. Boxall, J., Koh, C., Sloan, E., et al., 2012. Droplet Size Scaling of Water-In-Oil Emulsions under Turbulent Flow. *Langmuir* 28: 104–110.

8. Bradshaw, P., 1996. Turbulence Modeling with Application to Turbomachinery. *Progress in Aerospace Sciences* 32(6): 575–624.

9. Churchill, S.W., 1977. Friction-factor Equation Spans All Fluid-flow Regimes. *Chemical Engineering* 84(24): 91-92.

10. Croce, D., 2014. Study of Oil/Water Flow and Emulsion Formation in Electrical Submersible Pumps. MS Thesis, The University of Tulsa.

11. Euler, L., 1752. Maximes pour arranger le plus avantageusement les machines destinées à élever de l'eau par moyen des pompes (Maxims for arranging most advantageously machines intended to raise water by means of pumps), *Mémoires de l'Académie Royale des Sciences et des Belles Lettres à Berlin*, 8: 185-232.

12. Euler, L., 1754. Théorie plus complette des machines qui sont mises en mouvement par la rueáction de l'eau (More complete theory of machines that are set in motion by reaction with water), *Mémoires de l'Académie Royale des Sciences et des Belles Lettres à Berlin*, 10: 227-295.

13. Gamboa, J., and Prado, M., 2011. Review of Electrical-submersible-pump Surging Correlation and Models. *SPE Production & Operations*, 26(04): 314-324.

14. Gülich, J.F., 1999. Pumping Highly Viscous Fluids with Centrifugal Pumps – Part 1. *World Pumps* (395), 30–34.

15. Gülich, J.F., 1999. Pumping Highly Viscous Fluids with Centrifugal Pumps – Part 2. *World Pumps* (396), 39–42.

16. Gulich, J.F., 2007. *Centrifugal Pumps*. Berlin Heidelberg, Springer, New York.

17. Hinze, J.O., 1955. Fundamentals of the Hydrodynamic Mechanism of Splitting in Dispersion Processes. *AIChE Journal*, 1(3): 289-295.

18. Hole, G., 1994. Fluid Viscosity Effects on Centrifugal Pumps. *Pumps and Systems*, April 1994.

19. Hydraulic Institute. 1955. *Determination of Pump Performance when Handling Viscous Liquid*, tenth edition.

20. Ippen, A., 1946. The Influence of Viscosity on Centrifugal Pump Performance. *Trans. ASME 68*: 823-848.

21. Kirby, B.J., 2010. *Micro and Nanoscale Fluid Mechanics: Transport in Microfluidic Devgices*. Cambridge University Press.

22. Legendre, D., and Magnaudet, J., 1998. The Lift Force on a Spherical Bubble in a Viscous Linear Shear Flow. *Journal of Fluid Mechanics* 368: 81–126.

23. Li, W.G., 2000. The "Sudden-rising Head" Effect in Centrifugal Oil Pumps. *World Pumps*, 2000(409): 34-36.

24. Li, W.G., 2002. Experimental Investigation of Performance of Commercial Centrifugal Oil pump. *World Pumps,* 2002 (425), 26–28

25. Monte Verde, W., Biazussi, J., Bannwart, A., Arrifano Sassim, N., Estevam, V., 2013. Gas and Viscous Effects on the ESPs Performance. Proceedings of SPE Artificial Lift Conference-American, Cartagena, Colombia.

26. Morrison, G., Yin, W., Agarwal, R., and Patil, A., 2018. Development of Modified Affinity Law for Centrifugal Pump to Predict the Effect of Viscosity. *J. Energy Resour. Technol*. September 2018; 140(9): 092005

27. Ngan, K. 2010. Phase Inversion in Dispersed Liquid-liquid Pipe Flow. MSc Thesis, University College London.

28. Patil, A.V., and Morrison, G.L., 2017. Pump Affinity Laws Modified to Include Viscosity and Gas Effects. Proceedings of Turbomachinery and Pump Symposia, Houston, Texas.

29. Peters, F., and Arabali, D., 2013. Interfacial Tension between Oil and Water Measured with a Modified Contour Method. *Colloids and Surfaces A: Physicochemical and Engineering Aspects*. 426: 1–5.

30. Phan, H., Nguyen, T., Al-Safran, E., Saasen, A., Nes, O., 2017. An Experimental Investigation into the Effects of High Viscosity and Foamy Oil Rheology on a Centrifugal Pump Performance. *Journal of Petroleum Science and Technology*, 7(1), 67-78.

31. Solano, E.A., 2009. Viscous Effects on the Performance of Electro Submersible Pumps (ESP's). MSc Thesis, the University of Tulsa, Tulsa, OK.

32. Stepanoff, A.J., 1949. How Centrifugal Pumps Perform when Pumping Viscous Oils. *Power*. 85-87.

33. Stepanoff, A.J., 1957. *Centrifugal and Axial Flow Pump: Theory, Design, and Application, 2nd edition*. New York: John Wiley & Sons

34. Sun, D., and Prado, M.G., 2006. Single-phase Model for Electric Submersible Pump (ESP) Head Performance. *SPE Journal*, 11(01): 80-88.

35. White, F., 2005. *Viscous Fluid Flow, 3rd edition*. McGraw-Hill Series in Mechanical Engineering, McGraw-Hill Science.

36. Wiesner, F.J., 1967. A Review of Slip Factors off Centrifugal Impeller. *J. Eng. Power*, 89(4), 558-566.

37. Wood Group ESP, 2004. *Product Catalog*. Wood Group ESP, Inc, Oklahoma City, OK.

38. Zhang, H.-Q., 2013-2018. Proceedings of TUALP Spring Advisory Board Meeting, the University of Tulsa, Tulsa, OK.

39. Zhang, J., 2017. Experiments, CFD Simulation, and Modeling of ESP Performance under Viscous Fluid Flow Conditions. MSc Thesis. The University of Tulsa.

40. Zhu, H., Jianjun, Z., Rutter, R., Jiecheng, Z., & Zhang, H.-Q. (2018a). Sand Erosion Model Prediction, Selection and Comparison for Electrical Submersible Pump (ESP) using CFD Method. *Proceedings of the ASME 2018 5th Joint US-European Fluids Engineering Division Summer Meeting*. https://doi.org/10.1115/FEDSM2018-83179

41. Zhu, H., Zhang, J., Zhu, J., Rutter, R., & Zhang, H.-Q. (2019a). A Numerical Study of Turbulence Model and Rebound Model Effect on Erosion Simulations in an Electrical Submersible Pump (ESP). *Proceedings of the ASME 2019 ASME-JSME-KSME Joint Fluids Engineering Conference*. San Francisco, CA, USA, July 28-Aug 1: Paper No. AJKFLUIDS2019-5538. https://doi.org/10.1115/AJKFluids2019-5538

42. Zhu, H., Zhu, J., Rutter, R., & Zhang, H.-Q. (2019b). A Numerical Study on Erosion Model Selection and Effect of Pump Type and Sand Characters in Electrical Submersible Pumps (ESPs) by Sandy Flow. *Journal of Energy Resources Technology*, *141*(12), 122004. https://doi.org/10.1115/1.4044941

43. Zhu, H., Zhu, J., Zhang, J., & Zhang, H. Q. (2017a). Efficiency and Critical Velocity Analysis of Gravitational Separator through CFD Simulation. *Proceedings of the ASME International Mechanical Engineering Congress and Exposition*, https://doi.org/10.1115/IMECE2017-71230

44. Zhu, H., Zhu, J., Zhou, Z., Rutter, R., Forsberg, M., Gunter, S., & Zhang, H. Q. (2019c). Experimental Study of Sand Erosion in Multistage Electrical Submersible Pump ESP: Performance Degradation, Wear and Vibration. *Proceedings of the SPE International Petroleum Technology Conference*. https://doi.org/10.2523/IPTC-19264-MS

45. Zhu, H., Zhu, J., Zhou, Z., Rutter, R., & Zhang, H. Q. (2019d). Wear and Its Effect on Electrical Submersible Pump ESP Performance Degradation by Sandy Flow: Experiments and Modeling. *Proceedings of the Offshore Technology* Conference. https://doi.org/10.4043/29480-MS

46. Zhu, H. (2019). Experiments, CFD Simulation and Modeling of Sand Wear and Performance Degradation in ESPs. *Ph.D. Disertation*. University of Tulsa.

47. Zhu, J., Farfan, J. A. M., Zhang, J., Cuamatzi-Melendez, R., Zhu, H., & Zhang, H. Q. (2018b). Flow Pattern Prediction in Electrical Submersible Pump (ESP) under Gassy Flow Conditions using Transient Multiphase CFD Methods with Visualization Experimental Validation. *Proceedings of the ASME 2018 5th Joint US-European Fluids Engineering Division Summer Meeting*, https://doi.org/10.1115/FEDSM2018-83081

48. Zhu, J., Wang, Z., Zhu, H., Cuamatzi-Melendez, R., Martinez-Farfan, J. A., Jiecheng, Z., & Zhang, H. Q. (2018c). Mechanistic Modeling of Electrical Submersible Pump ESP Boosting Pressure under Gassy Flow Conditions and Experimental Validation. *Proceedings of the SPE Annual Technical Conference and Exhibition*.

49. Zhu, J., Zhang, J., Cao, G., Zhao, Q., Peng, J., Zhu, H., & Zhang, H. Q. (2019e). Modeling Flow Pattern Transitions in Electrical Submersible Pump under Gassy Flow Conditions. *Journal of Petroleum Science and Engineering*, *180*, 471–484.

https://doi.org/10.1016/j.petrol.2019.05.059

50. Zhu, J., Zhang, J., Zhu, H., & Zhang, H. Q. (2018d). A Mechanistic Model to Predict Flow Pattern Transitions in Electrical Submersible Pump under Gassy Flow Condition. *Proceedings of the SPE Artificial Lift Conference and Exhibition*. https://doi.org/10.2118/190927-MS
51. Zhu, J., Cao, G., Tian, W., Zhao, Q., Zhu, H., Song, J., Peng, J., Lin, Z., Zhang, H.Q. (2019f). Improved Data Mining for Production Diagnosis of Gas Wells with Plunger Lift through Dynamic Simulations. *Proceedings of SPE Annual Technical Conference and Exhibition*. https://doi.org/10.2118/196201-MS
52. Zhu, J., Zhu, H., Cao, G., Banjar, H., Peng, J., Zhao, Q., & Zhang, H.-Q. (2019g). A New Mechanistic Model for Oil-Water Emulsion Rheology and Boosting Pressure Prediction in Electrical Submersible Pumps ESP. *Proceedings of the SPE Annual Technical Conference and Exhibition*. https://doi.org/10.2118/196155-MS
53. Zhu, J., Zhu, H., Zhao, Q., Fu, W., Shi, Y., & Zhang, H. Q. (2019h). A Transient Plunger Lift Model for Liquid Unloading from Gas Wells. *Proceedings of SPE International Petroleum Technology Conference*. https://doi.org/10.2523/19211-MS
54. Zhu, J., Zhu, H., Cao, G., Zhang, J., Peng, J., Banjar, H., & Zhang, H. Q. (2019i). A New Mechanistic Model to Predict Boosting Pressure of Electrical Submersible Pumps ESPs under High-Viscosity Fluid Flow with Validations by Experimental Data. *Proceedings of the SPE Gulf Coast Section Electric Submersible Pumps Symposium*. https://doi.org/10.2118/194384-MS
55. Zhu, J., Zhu, H., Wang, Z., Zhang, J., Cuamatzi-Melendez, R., Farfan, J. A. M., & Zhang, H.-

Q. (2018e). Surfactant Effect on Air/Water Flow in a Multistage Electrical Submersible Pump (ESP). *Experimental Thermal and Fluid Science*, *98*, 95–111. https://doi.org/10.1016/j.expthermflusci.2018.05.013

56. Zhu, J., Zhu, H., Zhang, J., & Zhang, H. Q. (2017b). An Experimental Study of Surfactant Effect on Gas Tolerance in Electrical Submersible Pump (ESP). *Proceedings of the ASME International Mechanical Engineering Congress and Exposition*, https://doi.org/10.1115/IMECE2017-70165

57. Zhu, J., Zhu, H., Zhang, J., & Zhang, H. Q. (2019j). A Numerical Study on Flow Patterns inside an Electrical Submersible Pump (ESP) and Comparison with Visualization Experiments. *Journal of Petroleum Science and Engineering*, *173*, 339–350. https://doi.org/10.1016/j.petrol.2018.10.038

58. Zhu, J., Zhu, H., Cao, G., Zhang, J., Peng, J, Banjar, H., Zhang, H.-Q. (2019k). A New Mechanistic Model To Predict Boosting Pressure of Electrical Submersible Pumps Under High-Viscosity Fluid Flow with Validations by Experimental Data. *SPE Journal,* SPE-193384 (accepted). https://doi.org/10.2118/194384-PA

59. Zhu, J., Banjar, H., Xia, Z., and Zhang, H.-Q., 2016. CFD Simulation and Experimental Study of Oil Viscosity Effect on Multi-stage Electrical Submersible Pump (ESP) Performance. *Journal of Petroleum Science and Engineering*, 146, 735-745.

60. Zhu, J., Guo, X., Liang, F., and Zhang, H.-Q., 2017. Experimental Study and Mechanistic Modeling of Pressure Surging in Electrical Submersible Pump. *Journal of Natural Gas Science and Engineering*, 45: 625-636.

APPENDIX A

EQUIPMENT AND INSTRUMENT SPECIFICATIONS

Table A.1 TUALP High-Viscosity ESP Flow Loop Equipment Specifications

Equipment	**Model**	**Capacity**	**Purpose**
ESP Pump	GE Oil & Gas Wood Group TE-2700	BEP:2700 bpd, 3,500 rpm	Testing Bench
Electric Motor	North American H3650	50 hp	Drive Motor
Air Compressor	Kaeser CSD60	186 cfm, 217 psi	Air Source
Air Pressure Regulator	Speedaire 4ZM22	300 psi Max Inlet Pressure, 150 psi Max Outlet Pressure	Air Pressure Regulation
Variable Speed Drive	Hitachi L300P	50 hp	Altering Rotational Speed
ESP Thrust Chamber	Schlumberger REDA NO.88AB1- LT	-	Thrust Bearing Box
Liquid Pneumatic Control Valve	Fisher Body ED Actuator 657 Positioner 582i	-	Liquid Flow Rate Control
Water Pump	Dayton Stainless Steel Centrifugal Pump 2ZWT9A	0.5 hp	Water Circulation
Water Tank	Value Brand T-0300-059	300 gal	Water Storage
Water Pneumatic Control Valve	Fisher Body V100 Actuator 1052 Positioner 3622	-	Water Flow Rate Control

Table A.2 TUALP High-Viscosity ESP Flow Loop Instrumentation Specifications

Instrument	Model	Range	Accuracy
Thermocouple	Thermo Electric TCMSC83077875	0 to 1600 °F	±0.75%
Resistance Temperature Detector	Omega PR-11-2-100-1/8-18-E	-200 to 600 °C	±0.15°C
Temperature Transmitter	INOR IPAQ R520	-	-
Absolute Pressure Transmitter	Emerson Rosemount 2051	0 to 500 psi	±0.1%
Differential Pressure Transmitter	Emerson Rosemount 3051S	-10 to 50 psig	±0.1%
Pipe Viscometer	Emerson Rosemount 3051S	-250 to 250 psig	±0.1%
Coriolis High Flow Rate Meter	Proline Promass 80E	0 to 6615 lb/min	Mass Flow: ±0.2% Volume Flow: ±0.2% Density: ±0.0005 g/cm^3
Coriolis Low Flow Rate Meter	Micro Motion CMF200	0 to 1600 lb/min	Mass Flow: ±0.1% Volume Flow: ±0.1% Density: ±0.0005 g/cm^3

Table A.3 TUALP High-Viscosity ESP Flow Loop DAQ Specifications

Device	Features
Data Processing Computer	Dell Optiplex 9020, i7-4770 CPU @ 3.4 GHz, RAM: 16GB, HD: 1TB
National Instruments cFP-AI-110	• Eight analog voltage or current input channels • Eight voltage input ranges: 0–1 V, 0–5 V, 0–10 V, ±60 mV, ±300 mV, ±1 V, ±5 V, and ±10 V • Three current input ranges: 0–20, 4–20, and ±20 mA • 16-bit resolution • Three filter settings: 50, 60, and 500 Hz • 250 V_{rms} CAT II continuous channel-to-ground isolation, verified by 2,300 V_{rms} dielectric withstand test • –40 to 70 °C operation • Hot-swappable
National Instruments cFP-AI-111	• Sixteen single-ended analog current input channels • Three input ranges: ±20, 0–20, and 4–20 mA • 16-bit resolution

	• Three filter settings: 50, 60, and 500 Hz • Hot-swappable • 2300 V_{rms} transient overvoltage protection • –40 to 70 °C operation
National Instruments cFP-AO-200	• Eight 0–20 or 4–20 mA outputs • 0.5 mA over ranging • 12-bit resolution • Up to 1 kΩ load impedance (with 24 V loop supply) • Indicators for open current loops • Short-circuit protection • 2300 V_{rms} transient overvoltage protection between the inter-module communication bus and the I/O channels • –40 to 70 °C operation • Hot plug-and-play
National Instruments cFP-1804	• Network interface: 10 BaseT and 100 BaseTX Ethernet, IEEE802.3, 10/100 Mbps • One RS-232 (DCE) serial port, 300 to 115200 bps • 11 to 30 VDC, 20W • 2300 V_{rms} transient overvoltage protection • –40 to 70 °C operation
National Instruments cFP-CB-1	• cFP-CB-1 is designed for general-purpose and hazardous voltage1 operation with all Compact FieldPoint I/O modules • 36 terminals available • Tie-wrap anchors for wires • Color-coded V and C terminals for voltage supply and common connections • –40 to 70 °C operation

Table A.4 Coriolis Flow Meters Specifications

	High Flow Meter	**Low Flow Meter**
Model	Promass 80E	CMF200M
Brand	Endress+Hauser	Emerson
Meter Size (inch)	3	2
Accuracy	0.20%	0.25%
Accurate Measurement Range (bpd)	>1700	>150
Pressure Drop at 300 cP (psi)	12.2 at 10,000 bpd	13.7 at 2,100 bpd
Pressure Drop at 700 cP (psi)	18.8 at 10,000 bpd	25.6 at 2,100 bpd
Pressure Drop at 1000 cP (psi)	23.0 at 10,000 bpd	34.1 at 2,100 bpd

Table A.5 Pipe-in-Pipe Heat Exchanger Design Data

	Fluid
Heat Transfer Media	Water
Volume Flow Rate (bpd)	1940
Inlet Temperature (°C)	0
Outlet Temperature (°C)	1
Density (kg/m^3)	1001
Specific Heat (W/K)	4129
Viscosity (cP)	1.7
Thermal Conductivity (W/m·K)	0.570
Pressure Drop (psi)	0.00
Log Mean Temp Difference (°C)	34.25
Heat Transfer Rate (BTU/hr)	50375
Heat Transfer Area (ft^2)	21
Length (ft)	27

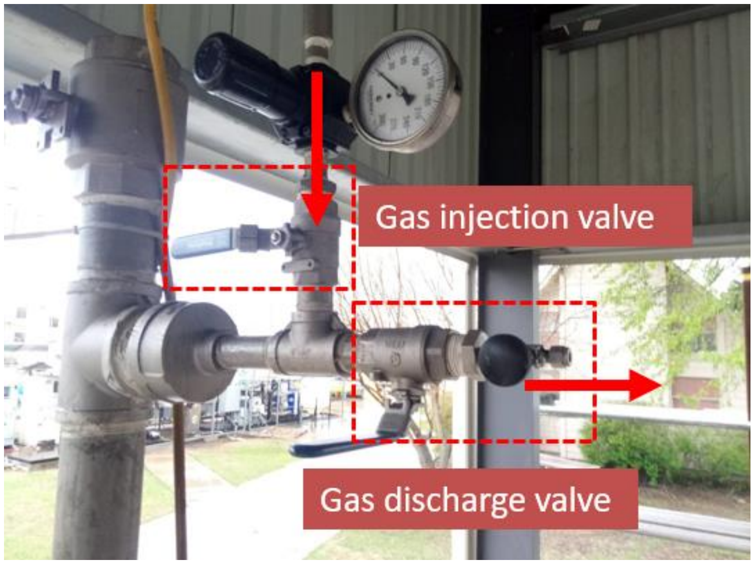

Figure A.1 Pressurization Port and Gas Discharge Valve

Figure A.2 Oil Injection Port

Figure A.3 Coriolis Flow Meter

Figure A.4 Temperature Sensor

Figure A.5 Temperature Sensor

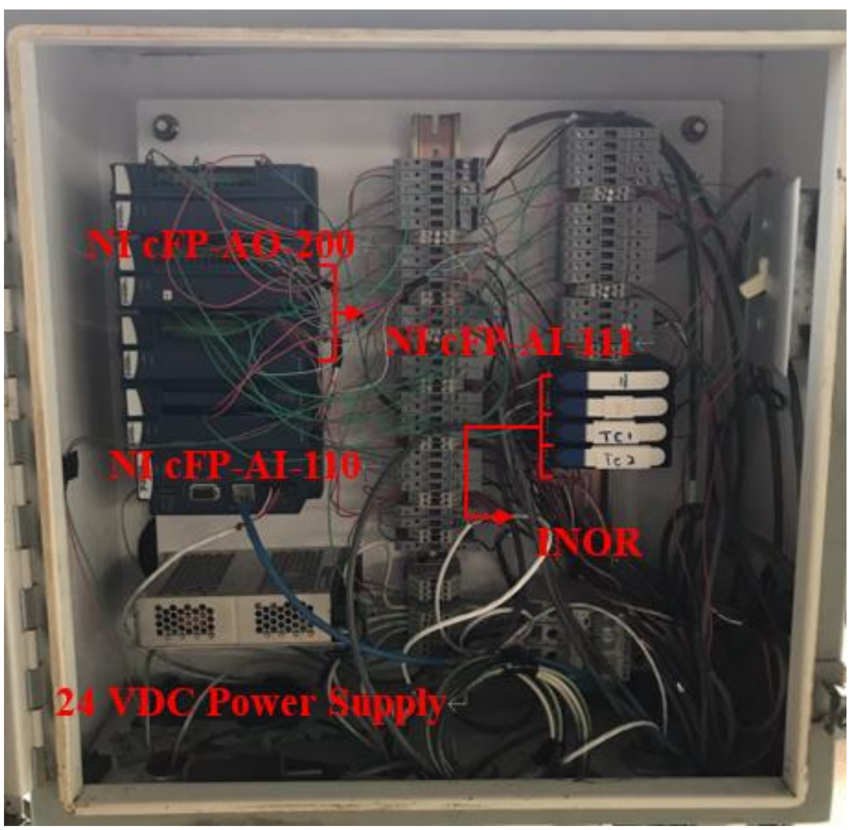

Figure A.6 Data Acquisition Device

Figure A.7 Pressure Monitors

Figure A.8 Pneumatic Control Valve

Figure A.9 Cooling System

Figure A.10 Pipe-in-Pipe Heat Exchanger

Figure A.11 Fluid Flow Schematic inside the Heat Exchanger

Figure A.12 Rotational Viscometer

Figure A.13 Water bath Temperature Control and Circulator

APPENDIX B

CHANNEL DISTRIBUTIONS OF NI MODULES

Table B.1 cFP-AI-110 Module #1 Channel Dsicturbutions

Channel	Description	Measurement Location
0	Not Used	
1	Rotational Speed	ESP Shaft
2	Not Used	
3	Not Used	
4	Not Used	
5	Not Used	
6	Not Used	
7	Not Used	

Table B.2 cFP-AI-111 Module #2 Channel Dsicturbutions

Channel	Description	Measurement Location
0	Differential Pressure	ESP Stage 6-7
1	Temperature	ESP Stage 14
2	Temperature	ESP Intake
3	Mass Flow Rate	Promass 80E
4	Fluid Density	Promass 80E
5	Mass Flow Rate	CMF200M
6	Fluid Density	CMF200M
7	Differential Pressure	ESP Stage 4-14
8	Not Used	
9	Not Used	
10	Not Used	
11	Not Used	
12	Differential Pressure	ESP Stage 4-5
13	Differential Pressure	ESP Stage 5-6
14	Temperature	Water Tank
15	Temperature	Coriolis Meter

Table B.3 cFP-AI-111 Module #3 Channel Dsicturbutions

Channel	Description	Measurement Location
0	Not Used	
1	Not Used	
2	Not Used	
3	Not Used	
4	Not Used	
5	Absolute Pressure	ESP Stage 8
6	Absolute Pressure	ESP Stage 9
7	Absolute Pressure	ESP Stage 10
8	Absolute Pressure	ESP Stage 11
9	Absolute Pressure	ESP Stage 12
10	Absolute Pressure	ESP Intake
11	Not Used	
12	Not Used	
13	Not Used	
14	Not Used	
15	Not Used	

Table B.4 cFP-AO-200 Module #4 Channel Dsicturbutions

Channel	Description
0	Liquid Control Valve
1	Variable Speed Drive
2	Water Control Valve
3	Not Used
4	Not Used
5	Not Used
6	Not Used
7	Not Used

APPENDIX C

PNEUMATIC CONTROL VALVE FLUCTUATION AND REPAIR

There were some problems with the viscosity experiment devices. The most important one was the pneumatic control valve. The seal in the pneumatic control valve was broken, thus causing a leak even if the valve is fully closed, leading to a large fluctuation at relative high mass flowrate before the seal replacement.

To test the sensitivity of the pneumatic control valve, the mass flow rate in a certain period at a certain valve opening was collected by the data acquisition system. In this test, 600 points were collected in 10 minutes, which means one point is acquired per second. The valve is regulated to be 0% closed (Qmax), 60% closed (0.4 Qmax), 80% closed (0.2 Qmax) and 90% closed (0.1 Qmax). The mass flow rate is assumed to be proportional to the valve opening degree. The collected mass flowrate is transferred to volume flowrate.

The figures below show the variation of the volume flowrate in 10 minutes. Figure C.1 shows the variation of volume flow rate when the valve is fully open (0% closed). A large fluctuation occurs during the time. The maximum value is about 2500 bpd while the minimum value is about 1227 bpd. The average value is 1728.77 bpd.

Figure C.2 shows the variation of volume flow rate when the valve is 90% closed. The volume flow rate is steady during the time.

Figure C.3 shows the comparison of volume flowrate variation when the valve is 0% closed and 60% closed. There is almost no difference between the two situations. Furthermore, the average volume flowrate is almost the same.

Figure C.4 shows the comparison of volume flowrate variation when the valve is 0% closed and 80% closed. There are no obvious differences between the two situations. Moreover, the average volume flowrate is 1728.77 bpd and 1611.87 bpd separately.

Figure C.5 shows the comparison of volume flowrate variation when the valve is 0% closed and 90% closed. Obvious differences can be seen between the two situations. This means only when the valve opening degree is more than 80% closed, the valve can be relatively sensitive while regulating.

From the previous experiments, it is confirmed that there is no big difference in the average volume flow rate when the valve is regulated from 0% closed to 80% closed. However, the average volume flowrate changes significantly during the process, from 80% closed to 100% closed off the valve.

The errors between the maximum/minimum volume flow rate and the average volume flow rate are shown in Table C.1. The biggest error can be about 30% at a high-volume flowrate while it reduces to about 17% at a low volume flow rate. Since the temperature is continuously increasing during the experiment (the water to cooling the oil was not used since the temperature was below zero), the viscosity of oil decreases during the time. Although the variation of viscosity will affect the volume flowrate, it cannot deny the fact that there are some problems with the valve.

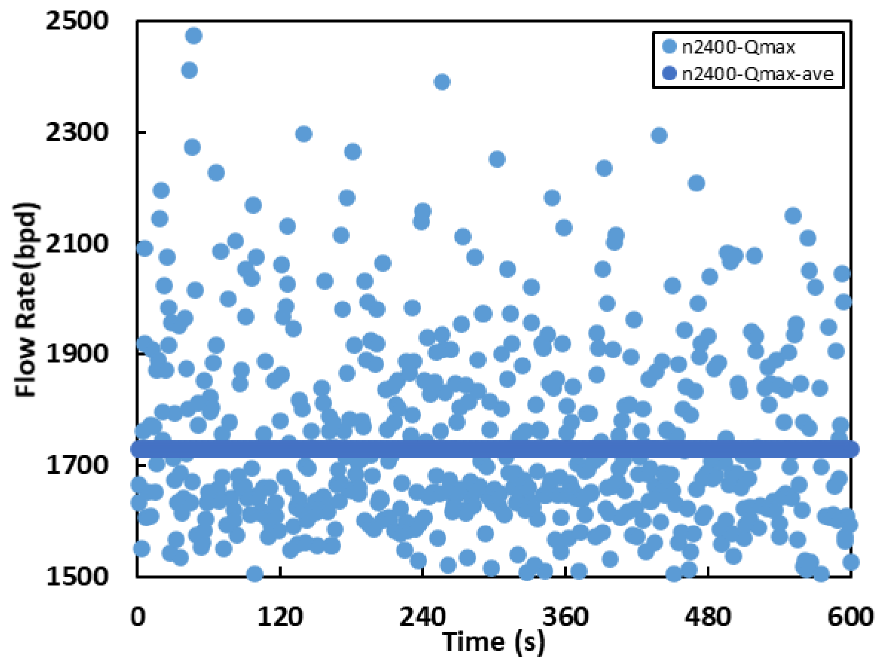

Figure C.1 The variation of volume flow rate when the valve is 0% closed

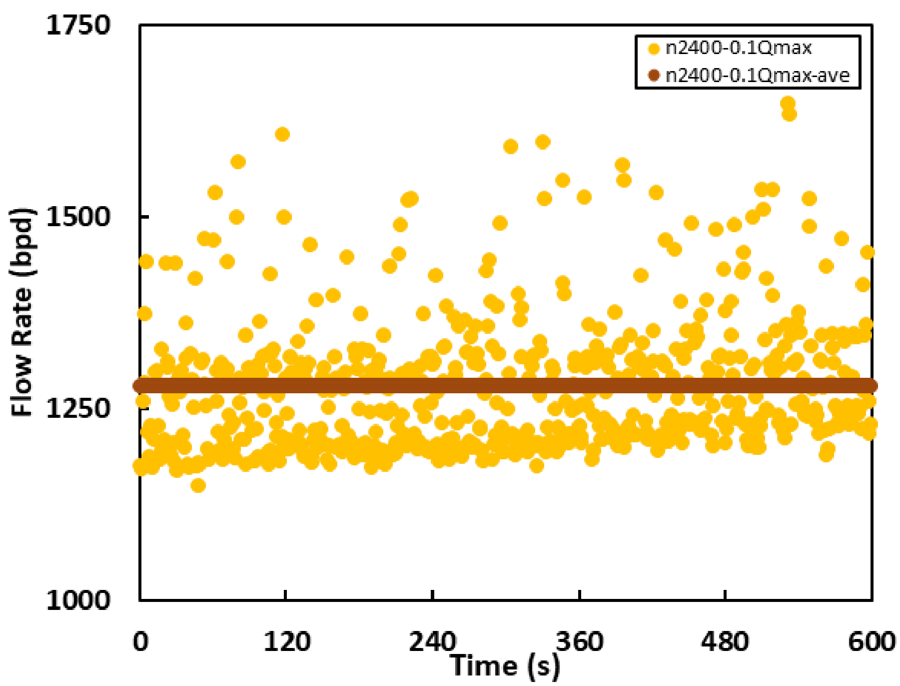

Figure C.2 The variation of volume flow rate when the valve is 90% closed

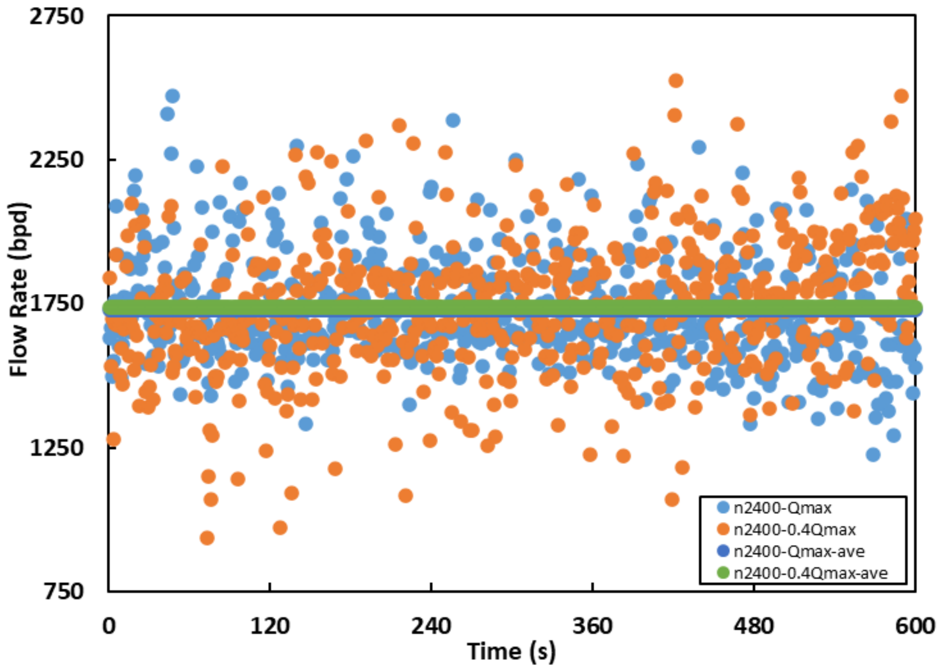

Figure C.3 The variation of volume flow rate when the valve is 0% and 60% closed

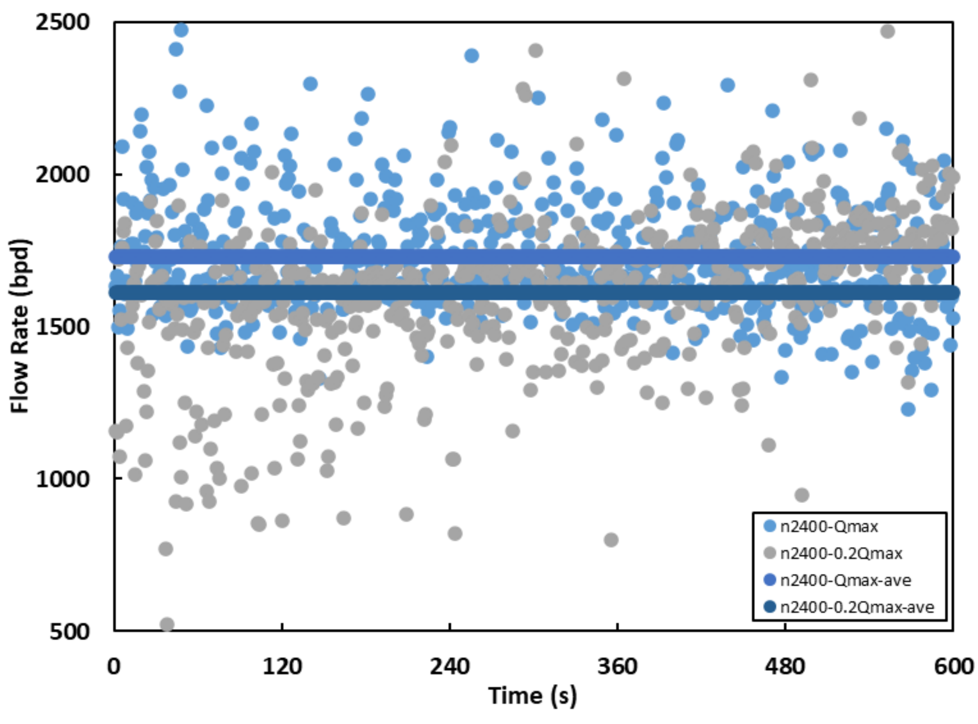

Figure C.4 The variation of volume flow rate when the valve is 0% and 80% closed

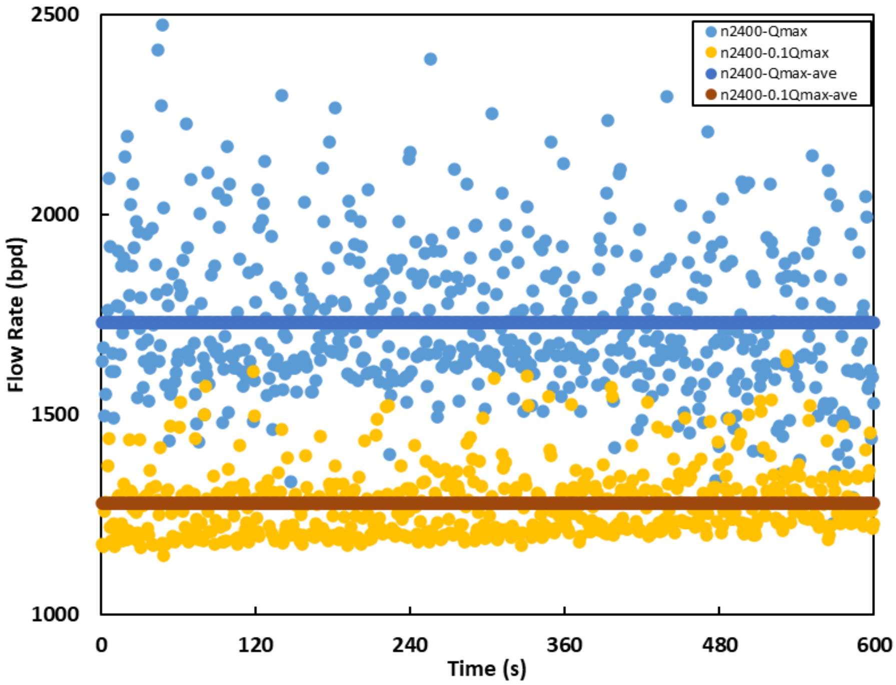

Figure C.5 The variation of volume flow rate when the valve is 0% and 90% closed

Table C.1 Errors in the maximum/minimum volume flow rate and the average volume flow rate

Volume flow rate	Qmax (bpd)	Qmin (bpd)	Ave (bpd)	Error max-ave (%)	Error min-ave (%)	Average viscosity (cP)
Qmax (0% closed)	2250	1500	1728.77	30.1503381	13.23310793	114.38
0.4 Qmax (60% closed)	2250	1500	1739.08	29.37875198	13.74749868	78.76
0.2 Qmax (80% closed)	2000	1250	1611.87	24.07948532	22.45032168	65.21
0.1 Qmax (90% closed)	1500	1170	1278.41	17.3332499	8.480065081	48.4

Some conclusions can be made about the pneumatic control valve:

1. The fluctuation is significant when the volume flow rate is high. Moreover, it becomes

steady when the volume flow rate is low.

2. The average volume flowrate changes little when the valve opening degree ranges from 0% closed to 80% closed and changes significantly when it ranges from 80% closed to 100% closed.

When the pneumatic valve was uninstalled and sent to be repaired, the flow rate is regulated by a manual valve. However, it is hard to close the manual valve at high rotational speed or low flowrate. Because of the pressure upstream, the valve is vibrating at high rotational speed and low flowrate. As a result, the maximum rotational speed is 2400 rpm. Figure C.6 shows how the experiment was conducted without the pneumatic control valve. The section of the pneumatic control valve was replaced by a temporary pipe to connect the flowmeter and the manual control valve to make sure the experimental facility remained a closed loop.

Figure C.6 Loop with Pneumatic Valve Uninstalled